Computer Modeling in Engineering & Sciences

Tech Science Press

https://doi.org/10.32604/cmes.2026.081147

ARTICLE

Williamson Nanofluid Flow and Transport in an Asymmetric Porous Tapered Channel under Multiple Slip Conditions Using Perturbation and Supervised Machine Learning Models

H. Kamlesh[1], E. P. Siva[1,*], P. Bathmanaban[2], O. D. Makinde[3] and Dharmendra Tripathi[4]

[1]Department of Mathematics, College of Engineering and Technology, SRM Institute of Science and Technology, Kattankulathur Campus, Chengalpattu Dt., Tamil Nadu, India

[2]Department of Science & Humanities (Mathematics), Jeppiaar Institute of Technology Kunnam, Sunguvarchatram, Sriperumbudur, Chennai, Tamil Nadu, India

[3]Faculty of Military Science, Stellenbosch University, Stellenbosch, South Africa

[4]Department of Mathematics, National Institute of Technology Uttarakhand, Srinagar, India

*Corresponding Author: E. P. Siva. Email: sivae@srmist.edu.in

Received: 06 March 2026; Accepted: 27 April 2026; Published: 27 May 2026

ABSTRACT: The current study comprehensively investigates Williamson nanofluid flow and transport in an asymmetric porous tapered channel under varying slip conditions, using both analytical and supervised machine learning approaches. This mathematical model integrates thermophoresis, Brownian motion, the Soret and Dufour effects, thermal radiation, and a transverse magnetic field to accurately describe thermosoluble transport phenomena relevant to biomedical contexts. The non-Newtonian Williamson formulation is used to explain how fluids, such as blood, dilute when sheared. Darcy resistance is used to describe porous structures in tissue scaffolds, capillary networks, and dialysis membranes. A perturbation method is used to find analytical solutions that show how key dimensionless parameters affect the profiles of velocity, temperature, concentration, Nusselt number, Sherwood number, skin friction, and pressure gradient. Supervised machine learning models, including artificial neural networks, are also used to predict heat and mass transfer properties and confirm analytical trends with a high degree of accuracy. The results show that increasing the Hartmann number reduces fluid motion due to Lorentz force resistance by approximately 14%, while the Williamson parameter increases shear-thinning and increases velocity by approximately 9%. Thermal radiation significantly broadens the temperature distribution, increasing heat transfer by 12%. The combination of perturbation analysis and supervised machine learning models demonstrates strong predictive power and makes the results more reliable. The integrated analytical-machine learning framework provides essential insights for enhancing nanoparticle-mediated drug delivery and advancing hyperthermia cancer treatment through regulated thermosolute transport in porous biological tissues.

KEYWORDS: Williamson nanofluid; magnetohydrodynamics (MHD); thermal radiation; hyperthermia cancer therapy; drug delivery; multiple slip boundary

1 Introduction

The study of non-Newtonian nanofluids in biomedical applications has generated considerable interest due to their potential roles in therapeutic drug delivery, cancer hyperthermia treatment, and regenerative tissue engineering. Blood is a non-Newtonian fluid, so use the Williamson rheological model, which accounts for its shear–thinning properties, as a likely way to model it. Incorporating nanoparticles into such fluids

improves mass and heat transfer, thereby enhancing biomedical processes. Then the MHD effect enhances fluid flow law, easing targeted drug delivery and thermal therapy for tumors. Within this structure, the slip dynamics of Williamson nanofluids into porous biological tissues have been investigated using a thorough mathematical formulation that integrates the impact of magnetic force, thermal radiation, and cross-diffusion wonders, including the Soret and Dufour devices. The proposed model improves the agreement of optimized medicinal delivery routes and refines thermal rule plans in clinical oncology. Also, an intelligent structure for analyzing and optimizing the complex actions displayed by non-Newtonian nanofluid systems is stable with the addition of machine learning (ML) models. Algorithms like Linear Regression, Logistic Regression, Naive Bayes, Support Vector Machine, Decision Tree, Random Forest, and Artificial Neural Network predict flow attributes, heat reactions, and ship efficacy. The validity of predictions is higher with this mixture of mathematical modeling and ML analysis, and biomedical and therapeutic applications are helped to be created by Akram et al. [1].

Non-Newtonian Williamson fluids have shear-thinning behavior and are viscoelastic in nature. Generally, nanofluids are used for targeted drug delivery. The typical volume fraction of nanofluid used for drug delivery ranges from 1% to 10%. The Williamson nanofluid enhances heat and mass transfer, has a higher viscosity, and exhibits increased thermal conductivity compared to the base fluid. Akram et al. [1] examined the effect of bio-Magnetohydrodynamics fields on peristaltic discharge in the double diffusive Williamson nanofluids. Nadeem and Akram [2] examined pressure variation and transfer dynamics in an asymmetric channel, featuring lubrication approximation assumptions to explain peristaltic qualities. Malik et al. [3] study the effect of magnetic parameters on the 3D flow of Williamson fluids across a linearly stretching surface. A mathematical model for the esophageal peristalsis of Williamson's bloodstream was generated (Farooq and Hussain [4]), which involved a solar-powered pumping system to imitate biological activity. Nadeem and Hussain [5] examined the 2D transport and thermal traits of a Williamson nanofluid on a stretching sheet featuring the impact of nanoparticle dispersal. The governing boundary-layer equations were devised, solved, and concluded by us to see how important physical parameters impact the temperature, velocity, and nanoparticle concentration profile. Akbar et al. [6] study nanofluid peristaltic flow within a tubular building featuring conformal boundaries, which was examined with a focus on investigative perspectives. Krishnamurthy et al. [7] investigated the impact of steady-state MHD on the boundary-layer growth of Williamson nanofluids in porous media and reactive mechanisms on the thermal radiation effects. Eldabe et al. [8] examined MHD-driven peristaltic transport of Williamson nanofluids through non-Darcy porous layers. Nadeem et al. [9] investigate the 2D flow of a Williamson fluid model over a stretching sheet.

Magnetohydrodynamic (MHD) nanoparticles are injected in blood for a Williamson fluid directly to tumors using magnetic fields for targeted drug delivery. A periodic magnetic field then heats these nanoparticles, generating localized hyperthermia (42°C–45°C) that kills cancer cells while sparing healthy tissue. This process uses MHD equations to balance fluid velocity, Joule heating, and nanoparticle concentration for optimal treatment. Hashim et al. [10] examined the mutual effects of Hartmann number and radiative heating on the thermal curve of Williamson nanofluids. Alharbi et al. [11] examined the transport of Williamson nanofluid in peristaltic figures and found it is influenced by the MHD and convective heating through the momentum integral method. Akram and Afzal [12] examined the interaction of induced Hartmann number, thermal buoyancy, and solutal buoyancy forces in the peristaltic movement of Williamson nanofluids through inclined channels. Chakradhar et al. [13] examined the effects of magnetic interactions on the wave-driven transport of Williamson fluids in porous tubes. Al-Khafajy [14] investigated the synergistic effects of magnetohydrodynamic forces and boundary wall constraints on the motion of Williamson fluid exhibiting variable viscosities within porous media. Riaz et al. [15] study both analytical and computational examinations of Williamson nanofluid dynamics in 2D asymmetric paths that were

supervised, integrating lubrication application, convective thermal flow mechanisms, and MHD effects. Makinde et al. [16] investigated the effect of thermal radiation on the magnetohydrodynamic peristaltic motion of a Walters-B fluid, taking into account internal heat generation and slip boundary effects.

The tumors, acting as porous media, exhibit Darcy resistance. The delivery of drugs facilitated by a Williamson blood nanofluid as it permeates through dense biological tissues is subject to precise physical drag. External magnetic fields are employed to overcome this porous resistance; they precisely guide and concentrate magnetic nanoparticles, intended for drug delivery, within the targeted tumor location. While the porous structure regulates heat dissipation, controlled hyperthermia is generated to destroy cancer cells. Ramesh and Devakar [17] examined the transport of MHD Walters B fluids induced by waves in confined inconsistent channels with heat transfer. Large eddy simulation for the investigation of flow dynamics, with a focus on slip boundary conditions, influences of Hartmann number, and appraisal of wave circulation velocity in relation to Weissenberg numbers, is undertaken. The peristaltic flow of a galvanic-obsessive Williamson fluid among a porous, contorted tube was investigated by Reddappa et al. [18], taking into account radiation effects on velocity and pressure distribution. Finally, shear stress and microrotation taken in the thermo-solute convection of micropolar flow compared to peristaltic movement were examined by Ravikumar and Makinde [19], taking into narrative cross-diffusion and thermohydrodynamic (THD) relations. Ramesh and Devakar [20] examined the effects of inclined magnetic forces on Williamson MHD transport in asymmetric porous geometries and their consequences for thermal distribution.

Williamson nanofluid investigates the asymmetric pathway flow, fluid dynamics, and kinetics of nanoparticles as they transport drugs through unconventional biological routes. In the field of drug delivery, this framework facilitates the prediction of the controlled dispersion, enhanced targeting, and efficient penetration of therapeutic agents. In cancer hyperthermia therapy, by optimizing heat distribution via nanoparticles, it becomes possible to selectively destroy tumor cells without damaging healthy tissues. Vajravelu et al. [21] investigated the non-Newtonian agent undergoing peristaltic movement through asymmetric channels with porous medium boundaries using a perturbation approach. Kavitha et al. [22] investigated the peristaltic transport of a Williamson fluid through an asymmetric porous channel based on the assumptions of long wavelength and low Reynolds number. Aly and Ebaid [23] investigated the peristaltic motion of nanofluids in asymmetric channels, integrating higher-order slip boundary conditions. Hayat et al. [24] investigated the peristaltic flow of Williamson fluids in inclined channels, focusing on the effects of oblique magnetic forces, conformal wall configuration, and cross-diffusion mechanisms (Soret and Dufour effects) on the temperature and concentration profiles. Recently, studies on viscoplastic nanofluid dynamics in various channel configurations have incorporated slip conditions, heat generation effects, and complex thermophysical phenomena to better understand transport behavior (Aich et al. [25]). An analytical inquiry of thermal energy transfer in biviscous flow undergoing peristaltic movement was accomplished. The MHD peristaltic actions of carbon nanotube suspenses in asymmetric channels were explored by Akbar et al. [26]. Concurrently, the peristaltic drip of Williamson fluids in inclined asymmetric channels was investigated by Akbar et al. [27], with partial thermal and slip conduction effects being studied.

In nanofluid flows, Williamson double diffusion describes the coupled transport of heat and mass driven by temperature and concentration gradients, encompassing effects such as Brownian motion and thermophoresis. In drug delivery, this mechanism facilitates controlled nanoparticle diffusion, thereby enhancing targeted delivery efficiency within biological tissues. Cancer hyperthermia therapy enables precise thermal regulation and nanoparticle distribution, effectively heating tumors while minimizing damage to surrounding healthy cells. Recently, researchers have garnered significant attention towards healthcare fluid flow phenomena, particularly about the robust convection of tertiary nanofluids across curved flexible layers within the context of peristaltic flow and double-diffusion effects, as demonstrated

by Alolaiyan et al. [28]. Tripathi et al. [29] investigated the influence of double diffusive forces on the peristaltic transport of a micropolar nanofluid through an asymmetric microchannel under electroosmotic conditions. A numerical investigation of double-diffusive transport in Williamson fluid flow bordering a vertical boundary was operated by Sushma et al. [30]. Mohamed et al. [31] examined the advancement of a fourth-grade nanofluid through porous media, focusing on the influences of magnetohydrodynamics, double-diffusion, viscous dissipation, and thermal generation or absorption. Saeed et al. [32] examined the peristaltic transport of Williamson nanomaterials in the context of heat radiation, involving multi-slippery barriers and magnetic fields. Bathmanaban et al. [33] investigated the double-diffusive convection and peristaltic transport of magnetized electroosmotic flow in a porous asymmetric channel filled with Casson nanofluid. Paandurangan et al. [34] examined double-diffusive mixed convection in heat and mass transmission inside Casson fluid. Bilal et al. [35] conducted recent research and analyzed the numerical aspects of theoretical magneto-Williamson nanofluid models, emphasizing the combined effects of viscous dissipation, bi-diffuse convection, thermal radiation, and multiple slip barriers.

Machine learning trained on surrogate solutions predicts Nu, Sh, and τ_w in Williamson nanofluid flows. While accurately modeling heat and mass transfer during drug delivery, it also reduces computational effort. This enhances the optimization of cancer hyperthermia treatment, thereby increasing therapeutic efficacy. The impact of Williamson fluid on radiation blood flow across an MHD cram was investigated by Priyadharshini and Karpagam [36], with a focus on mundane dependence and using a machine learning approach for multiple linear regression (MLR) to evaluate numerical values of the Nusselt number, skin friction, and Sherwood number. Research on classification problems [37] has evaluated several machine learning algorithms and assessed their performance and accuracy. Shafiq et al. [38] analyzed techniques for estimating the flow of unsteady hydromagnetic Williamson fluids over radiating surfaces, using both numerical approaches and artificial neural network models. Alzahrani et al. [39] investigated the Williamson ternary hybrid nanofluid thin film motion with heat and mass transfer under multiple slip effects on MHD within intelligent deep learning. Abbasi et al. [40] analyzed the flow of Williamson nanofluid, including non-linear radiation and chemical reactivity with motile microorganisms by artificial intelligence. Abbas et al. [41] examined the effects of heat radiation and flow dynamics of Prandtl ternary nanofluid over a Riga plate using artificial neural networks within the framework of a modified Buongiorno model. Shah et al. [42] examined the MHD water-based Prandtl nanofluid flow for thermal analysis on a stretching sheet utilizing a numerical-ANN framework. Jangid and Kolla [43] analyzed natural convection Williamson fluid flow over a vertical channel and the effects of magnetic and Soret using ANN modeling. Min et al. [44] study investigates a neural network-based model developed to analyze thermal-magnetic behavior in bioconvective Williamson nanofluids over a vertically stretching sheet, using accuracy with MSE and R^2 values in predicting. Vinutha et al. [45] examined Williamson nanofluid flow influenced by chemical reactions due to generated and absorbed heat using nonsimilar solutions by the finite element method. Hanumantha et al. [46] analyzed the heat and mass transfer characteristics of MHD Williamson hybrid nanofluid flow with activation energy effects in a porous asymmetric peristaltic channel. Ashique et al. [47] investigates the analysis of Williamson nanofluid over a moving wedge impact of homogeneous-heterogeneous, thermal radiation, and viscous dissipation in heat transfer using an artificial neural network-based flow.

The novelty of this study is to develop a comprehensive and physically consistent framework for Williamson nanofluid peristaltic transport. This extends beyond the limitations of existing models. Specifically, a new mathematical formulation is introduced for flow in an asymmetric porous tapered channel, which provides a more realistic representation of physiological transport in microvascular and biological systems. Unlike earlier studies that consider isolated effects, the present model simultaneously incorporates magnetohydrodynamic (MHD) forces, thermal radiation, double-diffusion phenomena (coupled

heat and mass transfer), thermophoresis, Brownian motion, and multi-slip boundary conditions within a unified framework. Previous literature has not collectively addressed this combined treatment of multiple interacting mechanisms.

Furthermore, this study analyzed skin friction, Nusselt number, and Sherwood number to understand deeper quantitative heat and mass transport characteristics relevant to biomedical processes such as targeted drug delivery and hyperthermia treatment. The nonlinear governing equations are solved analytically using a perturbation method. In addition, the work distinguishes itself by integrating multiple machine learning models to predict transport behavior, including Linear Regression, Logistic Regression, Naive Bayes, Support Vector Machine, Decision Tree, Random Forest, and Artificial Neural Network. To evaluate model accuracy, precision, recall, F1 score, and reliability using comprehensive statistical error analysis using MSE, MAE, and RMSE.

2 Mathematical Formulation

Fig. 1 shows the non-uniform wall structure that shows how a Williamson nanofluid flows through an asymmetric porous tapered channel. The left and right edges of the channel are shown by $H_1 = Y$ and $H_2 = Y$, and they are both asymmetric and irregular, like blood vessels or microfluidic drug delivery pathways in the body. The α angle is an inclined channel; also, gravitational components are the influence of $g \sin \alpha$ and $g \cos \alpha$ on flow behavior. The magnetohydrodynamic (MHD) effects of a uniform magnetic field (B_0) are perpendicular to the flow direction. The resistance to flow within the channel governs the porous medium, which is significant in modeling biological tissues. Boundary values of temperature, solute concentration, and nanoparticle fraction at the left wall are (T_0, C_0, H_0), while at the right wall they are (T_1, C_1, H_1). The velocity field for this two-dimensional bidirectional flow can be written as:

$$\vec{V} = (U(X, Y, t'),\ V(X, Y, t'),\ 0) \tag{1}$$

The heat transfer equation accounts for both viscous heating and radiative effects. The Dufour and Soret effects explain the interrelated dynamics of thermal and solute gradients. This model is useful for hyperthermia cancer treatment, which uses nanoparticles to move, diffuse, and have thermal effects; uses controlled heat transfer to kill cancer cells; and uses targeted drug delivery to make treatment more effective in complex biological channels.

The mathematical representation of the two channel boundaries is expressed according to the formulation suggested by Akram et al. [1], Paandurangan et al. [34]:

$$Y = H_1 = d_1 + mX + a_1 \sin\left(\frac{2\pi}{\lambda}(X - ct) + \phi\right) \quad \text{(Left Wall)} \tag{2}$$

$$Y = H_2 = -d_2 - mX - a_2 \sin\left(\frac{2\pi}{\lambda}(X - ct)\right) \quad \text{(Right Wall)} \tag{3}$$

In this case, λ is the wavelength, and a_1 and a_2 are the amplitudes of the left and right channel walls, respectively. The parameter m ($m \ll 1$) describes how the channel loses energy at its ends. The time variable is t, the phase difference is $0 \le \phi \le \pi$, and the wave speed is c. When $\phi = 0$, the channel is symmetric, meaning that both walls move in and out at the same time. These parameters must satisfy the following conditions:

$$a_1^2 + a_2^2 + 2a_1 a_2 \cos\phi \le 4d^2 \tag{4}$$

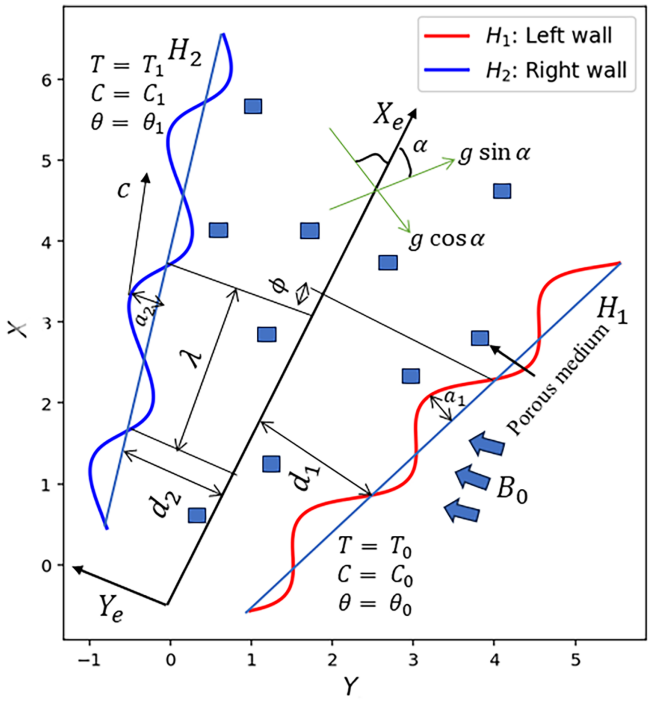

Figure 1: Geometry of an asymmetric channel with structured walls.

The stress tensor of Williamson fluid model's is given by Nadeem et al. [9], Jangid and Kolla [43], Ashique et al. [47] the following:

$$\boldsymbol{\tau} = \left[\mu_\infty + \frac{(\mu_0 - \mu_\infty)}{(1 - \Gamma\dot{\gamma})}\right] \mathbf{A_1} \tag{5}$$

In this case, $\boldsymbol{\tau}$ is the extra stress tensor, μ_0 is the zero shear rate viscosity, μ_∞ is the infinite shear rate viscosity, Γ is the time constant, $\mathbf{A_1} = \nabla\vec{V} + (\nabla\vec{V})^T$ is the first Rivlin-Erickson tensor (^{T} stands for transpose).

The mathematical definition of the shear rate $\dot{\gamma}$ is:

$$\dot{\gamma} = \sqrt{\frac{1}{2}\Pi} \tag{6}$$

where $\Pi = tr(\mathbf{A_1}^2)$, the invariant second strain tensor. Here we consider the case for which $\mu_\infty = 0$ and $\Gamma\dot{\gamma} < 1$, Eq. (5) reduces to yield the stress tensor in the form:

$$\boldsymbol{\tau} = \left[\frac{\mu_0}{(1 - \Gamma\dot{\gamma})}\right] \mathbf{A_1} = \mu_0 \left[1 + \Gamma\dot{\gamma}\right] \mathbf{A_1} \tag{7}$$

3 Governing Equations

A set of interconnected partial differential equations describing mass continuum, momentum dynamics, thermal energy distribution, and species diffusion governs the physical system. These mathematical models have been developed based on incompressible, laminar, and time-dependent flows while also incorporating the effects of thermal and solute buoyancy. Akram et al. [1], Eldabe et al. [8], Ramesh and

Devakar [20], Bathmanaban et al. [33], Paandurangan et al. [34] and Bilal et al. [35] applied magnetic fields and nanoparticle dynamics.

$$\frac{\partial U}{\partial X}+\frac{\partial V}{\partial Y}=0 \tag{8}$$

$$\begin{aligned}\rho_f\left(\frac{\partial U}{\partial t'}+U\frac{\partial U}{\partial X}+V\frac{\partial U}{\partial Y}\right)=&-\frac{\partial p'}{\partial X}+\frac{\partial \tau_{XX}}{\partial X}+\frac{\partial \tau_{XY}}{\partial Y}-\sigma B_0^2U-\frac{\mu}{k_0}U\\&+\rho g\left[(1-\theta_0)\rho_\beta\left(\beta_T(T-T_0)+\beta_C(\bar{C}-C_0)\right)\right]\\&-\rho g\left[(\rho_p-\rho_f)(\theta-\theta_0)\right]+\rho g\sin\alpha\end{aligned} \tag{9}$$

$$\rho_f\left(\frac{\partial V}{\partial t'}+U\frac{\partial V}{\partial X}+V\frac{\partial V}{\partial Y}\right)=-\frac{\partial p'}{\partial Y}+\frac{\partial \tau_{XY}}{\partial X}+\frac{\partial \tau_{YY}}{\partial Y}-\frac{\mu}{k_0}V-\rho g\cos\alpha \tag{10}$$

$$\begin{aligned}(\rho c_p)_f\left(\frac{\partial T}{\partial t'}+U\frac{\partial T}{\partial X}+V\frac{\partial T}{\partial Y}\right)=&\,k\left(\frac{\partial^2T}{\partial X^2}+\frac{\partial^2T}{\partial Y^2}\right)+D_{TC}\left(\frac{\partial^2C}{\partial X^2}+\frac{\partial^2C}{\partial Y^2}\right)\\&-\frac{\partial q_r}{\partial Y}+Q_0+(\rho c_p)_fD_B\left[\frac{\partial T}{\partial X}\frac{\partial \Theta}{\partial X}+\frac{\partial T}{\partial Y}\frac{\partial \Theta}{\partial Y}\right]\\&+(\rho c_p)_f\frac{D_T}{T_0}\left[\left(\frac{\partial T}{\partial X}\right)^2+\left(\frac{\partial T}{\partial Y}\right)^2\right]\end{aligned} \tag{11}$$

$$\frac{\partial C}{\partial t'}+U\frac{\partial C}{\partial X}+V\frac{\partial C}{\partial Y}=D_S\left(\frac{\partial^2C}{\partial X^2}+\frac{\partial^2C}{\partial Y^2}\right)+D_{TC}\left(\frac{\partial^2T}{\partial X^2}+\frac{\partial^2T}{\partial Y^2}\right) \tag{12}$$

$$\frac{\partial \Theta}{\partial t'}+U\frac{\partial \Theta}{\partial X}+V\frac{\partial \Theta}{\partial Y}=D_B\left(\frac{\partial^2\Theta}{\partial X^2}+\frac{\partial^2\Theta}{\partial Y^2}\right)+\frac{D_T}{T_{0_e}}\left(\frac{\partial^2T}{\partial X^2}+\frac{\partial^2T}{\partial Y^2}\right) \tag{13}$$

The additional stress tensor that accompanies the Williamson fluid model has the following additional parts:

$$\tau_{XX}=2\mu_0(1+\dot{\Gamma})\frac{\partial U}{\partial X} \tag{14}$$

$$\tau_{XY}=\mu_0(1+\dot{\Gamma})\left(\frac{\partial U}{\partial Y}+\frac{\partial V}{\partial X}\right) \tag{15}$$

$$\tau_{YY}=2\mu_0(1+\dot{\Gamma})\frac{\partial V}{\partial Y} \tag{16}$$

$$\tau_{XZ}=\tau_{YZ}=\tau_{ZX}=\tau_{ZY}=\tau_{ZZ}=0$$

Mathematically, the shear rate is $\dot{\gamma}$:

$$\dot{\gamma}=2\left[\left(\frac{\partial U}{\partial X}\right)^2+\left(\frac{\partial V}{\partial Y}\right)^2+\left(\frac{1}{2}\left(\frac{\partial U}{\partial Y}+\frac{\partial V}{\partial X}\right)\right)^2\right]^{1/2} \tag{17}$$

The Rosseland diffusion approximation is used to model radiative heat flux, shown as

$$q_r=-\frac{4\sigma_e^*}{3k_e^*}\frac{\partial T^4}{\partial Y}, \tag{18}$$

where σ^* represents the Stefan-Boltzmann constant and k^* represents the mean absorption coefficient. To make the non-linear relationship with temperature easier to understand, we use the Taylor series expansion of T^4 around the reference temperature T_0:

$$T^4 = T_0^4 + 4T_0^3(T - T_0) + 6T_0^2(T - T_0)^2 + \cdots \tag{19}$$

By Neglecting higher powers terms $(T - T_0)$, the shortened form the expansion reduces the following:

$$T^4 = -3T_0^4 + 4T_0^3 T \tag{20}$$

Substituting Eq. (20) in Eq. (18), we following:

$$q_r = -\frac{16\sigma_e^* T_0^3}{3k^*}\frac{\partial T}{\partial Y} \tag{21}$$

Differentiating Eq. (21) with respect to Y, we get

$$\frac{\partial q_r}{\partial Y} = -\frac{16\sigma^* T_0^3}{3k^*}\frac{\partial^2 T}{\partial Y^2} \tag{22}$$

To reduce the governing equations, we assume the non-dimensional quantities as

$$x = \frac{X}{\lambda}, \quad y = \frac{Y}{d}, \quad t = \frac{ct'}{\lambda}, \quad u = \frac{U}{c}, \quad v = \frac{V}{c}, \quad p = \frac{d^2 p'}{\mu c \lambda}, \quad h_1 = \frac{H_1}{d_1}, \quad h_2 = \frac{H_2}{d_1},$$
$$\delta = \frac{d}{\lambda}, \quad a = \frac{a_1}{d_1}, \quad b = \frac{a_2}{d_2}, \quad d = \frac{d_2}{d_1}, \quad Re = \frac{\rho_f c d}{\mu}, \quad Pr = \frac{\mu}{\rho_f \alpha_m}, \quad \nu = \frac{\mu}{\rho_f}, \quad \alpha_m = \frac{k}{(\rho C_p)_f},$$
$$M^2 = \frac{\sigma d^2 B_0^2}{\mu}, \quad Fr = \frac{c^2}{gd}, \quad \tau_{xx} = \frac{\lambda \tau_{XX}}{\mu c}, \quad \tau_{xy} = \frac{d\tau_{XY}}{\mu c}, \quad \tau_{yy} = \frac{d\tau_{YY}}{\mu c}, \quad Sc_1 = \frac{\nu}{D_s},$$
$$Sc_2 = \frac{\nu}{D_B}, \quad Da = \frac{k_0}{d^2}, \quad G_r = \frac{gd^2\rho_f\beta_T(1-\theta_0)(T_1 - T_0)}{\mu c}, \quad \theta = \frac{T - T_0}{T_1 - T_0}, \quad \sigma = \frac{C - C_0}{C_1 - C_0}$$
$$G_c = \frac{g(1-\theta_0)\rho_f\beta_C d^2(C_1 - C_0)}{\mu c}, \quad G_f = \frac{g(\rho_p - \rho_f)(\theta_1 - \theta_0)d^2}{\mu c}, \quad Rn = \frac{16\sigma^* T_0^3}{3\kappa^*(\mu c)_f},$$
$$N_{TC} = \frac{\tau D_{TC}(C_1 - C_0)}{\alpha_m(T_1 - T_0)}, \quad N_{CT} = \frac{D_{CT}(T_1 - T_0)}{D_s(C_1 - C_0)}, \quad N_b = \frac{\tau D_B(\Theta_1 - \Theta_0)}{\alpha_m}, \quad \gamma = \frac{\Theta - \Theta_0}{\Theta_1 - \Theta_0}$$
$$N_t = \frac{\tau D_T(T_1 - T_0)}{T_0 \alpha_m}, \quad u = \frac{\partial \psi}{\partial y}, \quad v = -\delta\frac{\partial \psi}{\partial x}, \quad We = \Gamma\frac{c}{\lambda}, \quad \beta = \frac{Q_0 d_1^2}{(T_1 - T_0)\mu C_p}. \tag{23}$$

The low Reynolds number approximation $(Re \approx 0)$ and lubrication approach $(\delta \ll 1)$, substituting of Eq. (23) into Eqs. (8)–(13), the governing equations simplify to:

$$0 = -\frac{\partial p}{\partial x} + \frac{\partial}{\partial y}\left[\left(1 + We\frac{\partial^2 \psi}{\partial y^2}\right)\frac{\partial^2 \psi}{\partial y^2}\right] - \left(M^2 + \frac{1}{Da}\right)\frac{\partial \psi}{\partial y}$$
$$+ G_r\theta + G_c\sigma - G_f\gamma + \frac{Re}{Fr}\sin\alpha \tag{24}$$

$$0 = -\frac{\partial p}{\partial y} \tag{25}$$

$$0 = (1 + Rn)\theta_{yy} + N_b\gamma_y\theta_y + N_t\theta_y^2 + N_{TC}\sigma_{yy} + \beta \tag{26}$$

$$0 = \sigma_{yy} + N_{CT}\theta_{yy} \tag{27}$$

$$0 = \gamma_{yy} + \frac{N_t}{N_b}\theta_{yy} \tag{28}$$

Eliminating pressure from Eqs. (24) and (25) yields the following:

$$\frac{\partial^2}{\partial y^2}\left[\left(1+We\frac{\partial^2\psi}{\partial y^2}\right)\frac{\partial^2\psi}{\partial y^2}\right]-\left(M^2+\frac{1}{Da}\right)\frac{\partial^2\psi}{\partial y^2}+G_r\frac{\partial\theta}{\partial y}+G_c\frac{\partial\sigma}{\partial y}-G_f\frac{\partial\gamma}{\partial y}=0 \tag{29}$$

The following non-dimensional boundary conditions are charged at the channel walls by the system. $y = h_1(x) = -1 - mx - a_1\sin\big(2\pi(x-t)+\phi\big)$ and $y = h_2(x) = 1 + mx + a_2\sin\big(2\pi(x-t)\big)$, the stream function and its normal derivative satisfy (Saeed et al. [32]).

$$\psi = \frac{F}{2}, \qquad \frac{\partial\psi}{\partial y} = l_1 S_{xy} - 1, \qquad y = h_1(x), \tag{30}$$

$$\psi = -\frac{F}{2}, \qquad \frac{\partial\psi}{\partial y} = -l_1 S_{xy} - 1, \qquad y = h_2(x), \tag{31}$$

$$\theta + l_2\frac{\partial\theta}{\partial y} = 0, \qquad \sigma + l_3\frac{\partial\sigma}{\partial y} = 0, \qquad \gamma + l_4\frac{\partial\gamma}{\partial y} = 0, \qquad y = h_1(x), \tag{32}$$

$$\theta - l_2\frac{\partial\theta}{\partial y} = 1, \qquad \sigma - l_3\frac{\partial\sigma}{\partial y} = 1, \qquad \gamma - l_4\frac{\partial\gamma}{\partial y} = 1, \qquad y = h_2(x) \tag{33}$$

In this case, l_1, l_2, l_3, and l_4 represent the velocity gradient, temperature gradient, solutal concentration gradient, and nanoparticle drift parameters, respectively. If $l_1 = l_2 = l_3 = l_4 = 0$, then the above parameters indicate that there is no drift condition. The average flow rate at the same location during the entire wave cycle is defined as:

$$Q_1 = \frac{1}{T}\int_0^T \bar{Q}\,dt \tag{34}$$

In a wave-stabilized coordinate system, the volume flow rate can be stated as

$$Q_1 = q + a_1 c\sin\left(\frac{2\pi}{\lambda}(X-ct)+\phi\right) + a_2 c\sin\left(\frac{2\pi}{\lambda}(X-ct)\right), \tag{35}$$

where q represents the mean flow contribution. In this framework, the nondimensional volume flux is defined as

$$q = \int_{h_1}^{h_2} u(x,y)\,dy, \tag{36}$$

where $u(x,y)$ is the axial velocity portion. When using non-dimensional variables, the wave coordinate system represents the volume flow rate as Q. A generalized parameter F is defined to establish a link with the stationary reference frame, connecting the flow rates in both frames as follows:

$$F = \frac{Q_1}{cd} = \frac{q}{cd}. \tag{37}$$

The instantaneous nondimensional flux can then be expressed in the form

$$F(x,t) = Q + a_1\sin(2\pi(x-t)+\phi) + a_2\sin(2\pi(x-t)), \tag{38}$$

where the parameters $a = \frac{a_1}{d_1}$ and $b = \frac{a_2}{d_1}$ represent the scaled wave amplitudes. An alternative representation of the nondimensional flow rate F can be written using the stream function as

$$F = \int_{h_1}^{h_2} u\, dy = \int_{h_1}^{h_2} \frac{\partial \psi}{\partial y}\, dy = \psi(h_2) - \psi(h_1). \tag{39}$$

The average pressure increment over a wavelength, denoted by Δp, is calculated as the space-time average of the pressure gradient along the lowest boundary.

$$\Delta p = \int_0^1 \int_0^1 \left(\frac{\partial p}{\partial x}\right)_{y=0} dx\, dt. \tag{40}$$

3.1 Perturbation Solution

The perturbation method is used to find an approximate solution to the boundary value problem (BVP) described in Eqs. (29)–(31). This method works for fairly small values of the Weissenberg number (We). Thus, the flow variables are written as a power series in terms of We:

$$\psi = \psi_0 + We \cdot \psi_1 + O(\psi_2) \tag{41}$$

$$p = p_0 + We \cdot p_1 + O(p_2) \tag{42}$$

$$F = F_0 + We \cdot F_1 + O(F_2) \tag{43}$$

By substituting the above series expansions into Eqs. (29) and (24), along with the limiting conditions in Eqs. (30)–(31), we get the following system:

3.2 Zeroth-Order Structure for We^0

$$\frac{\partial^4 \psi_0}{\partial y^4} = T_1^2 \frac{\partial^2 \psi_0}{\partial y^2} - G_r \frac{\partial \theta}{\partial y} - G_c \frac{\partial \sigma}{\partial y} + G_f \frac{\partial \gamma}{\partial y} \tag{44}$$

$$\frac{\partial p_0}{\partial x} = \frac{\partial^3 \psi_0}{\partial y^3} - T_1^2 \frac{\partial \psi_0}{\partial y} + G_r \theta + G_c \sigma - G_f \gamma + \frac{Re}{Fr} \sin \alpha \tag{45}$$

$$\psi_0 = \frac{F_0}{2}, \qquad y = h_1(x), \tag{46}$$

$$\psi_0 = -\frac{F_0}{2}, \qquad y = h_2(x), \tag{47}$$

$$\frac{\partial \psi_0}{\partial y} = l_1 \frac{\partial^2 \psi_0}{\partial y^2} - 1, \qquad y = h_1(x), \tag{48}$$

$$\frac{\partial \psi_0}{\partial y} = -l_1 \frac{\partial^2 \psi_0}{\partial y^2} - 1, \qquad y = h_2(x). \tag{49}$$

3.3 First-Order Structure for We^1

$$\frac{\partial^4 \psi_1}{\partial y^4} = -\frac{\partial^2}{\partial y^2}\left(\frac{\partial^2 \psi_0}{\partial y^2}\right) + T_1^2 \frac{\partial^2 \psi_1}{\partial y^2} \tag{50}$$

$$\frac{\partial p_1}{\partial x} = \frac{\partial}{\partial y}\left[\frac{\partial^2 \psi_1}{\partial y^2} + \left(\frac{\partial \psi_0}{\partial y}\right)^2\right] + T_1^2 \frac{\partial \psi_0}{\partial y} \tag{51}$$

$$\psi_1 = -\frac{F_1}{2}, \qquad y = h_1(x), \tag{52}$$

$$\psi_1 = \frac{F_1}{2}, \qquad y = h_2(x), \tag{53}$$

$$\frac{\partial \psi_1}{\partial y} = l_1 \left[\frac{\partial^2 \psi_1}{\partial y^2} + \left(\frac{\partial^2 \psi_1}{\partial y^2} \right)^2 \right], \qquad y = h_1(x), \tag{54}$$

$$\frac{\partial \psi_1}{\partial y} = -l_1 \left[\frac{\partial^2 \psi_1}{\partial y^2} + \left(\frac{\partial^2 \psi_1}{\partial y^2} \right)^2 \right], \qquad y = h_2(x). \tag{55}$$

4 Analytical Solution

To analyze the heat and mass transfer in the asymmetric channel, the stream function, pressure gradient, temperature, solutal concentration, and nanoparticle concentration distribution.

$$\psi_0(y) = f_7 + f_8 \cdot y + f_9 \cdot e^{T_1 y} + f_{10} \cdot e^{-T_1 y} + T_5 \cdot e^{-R_8 y} + T_6 \cdot y^2 \tag{56}$$

$$\psi_1(y) = f_{11} + f_{12} \cdot y + f_{13} \cdot e^{T_1 y} + f_{14} \cdot e^{-T_1 y} + T_{14} \cdot y \cdot e^{T_1 y} + T_{15} \cdot y \cdot e^{-T_1 y} + T_{16} \cdot e^{-R_8 y} \tag{57}$$

$$\psi(y) = \psi_0(y) + We \cdot \psi_1(y) \tag{58}$$

$$\frac{dp_0}{dx} = G_r \cdot \theta(y) + G_c \cdot \sigma(y) - G_f \cdot \gamma(y) + E_1 \cdot e^{-R_8 y} + E_2 \cdot y + E_3 \tag{59}$$

$$\frac{dp_1}{dx} = E_4 \cdot e^{T_1 y} + E_5 \cdot e^{-T_1 y} + E_6 \cdot e^{-R_8 y} + E_7 \cdot y \cdot e^{T_1 y} + E_8 \cdot y \cdot e^{-T_1 y} \tag{60}$$

$$\frac{dp}{dx} = \frac{dp_0}{dx} + We \cdot \frac{dp_1}{dx} \tag{61}$$

$$\theta(y) = f_5 + f_6 \cdot e^{-R_1 y} + R_3 y \tag{62}$$

$$\sigma(y) = f_2 + f_1 \cdot y - N_{CT} \cdot \theta(y) \tag{63}$$

$$\gamma(y) = f_4 + f_3 \cdot y - \frac{N_t}{N_b} \cdot \theta(y) \tag{64}$$

Skin Friction, Heat Transfer, and Mass Transfer Rates

Skin friction (τ_w), Nusselt number (Nu), and Sherwood number (Sh) are dimensionless parameters that are used to measure how effectively momentum, heat, and mass are transferred at a boundary. τ_w is the ratio of wall shear stress to dynamic pressure, and shear stress is directly proportional to the velocity gradient. Nu is the ratio of convective heat transfer to conductive heat transfer across the boundary. Sh is the ratio of convective mass transfer to diffusive mass transfer, making it the mass-transfer analogy to the Nusselt number.

$$\tau_w = \frac{\partial h_2}{\partial x} \cdot \frac{\partial^2 \psi}{\partial y^2}\bigg|_{y=h_2}, \qquad Nu = (1 + Rn) \frac{\partial h_2}{\partial x} \cdot \frac{\partial \theta}{\partial y}\bigg|_{y=h_2}, \qquad Sh = \frac{\partial h_2}{\partial x} \cdot \frac{\partial \sigma}{\partial y}\bigg|_{y=h_2}. \tag{65}$$

5 Results and Discussion

This section presents an analytical study of how key regulatory factors affect the temperature field, solute concentration, nanoparticle transport, and velocity distribution. Python is used to solve dimensionless regulatory equations to accurately and quickly calculate the resulting flow characteristics. The developed

formulation, based on low Reynolds number and quasi-steady peristaltic motion, captures the fundamental characteristics of coupled heat and mass transfer in complex biological systems. This method is particularly useful for biomedical engineering applications, such as targeted drug delivery, therapies using nanoparticles, and controlling temperature in cancer treatment using hyperthermia.

$$a_1 = 0.2, \quad a_2 = 0.1, \quad \phi = \frac{\pi}{2}, \quad x = 0.5, \quad d_1 = 1.0, \quad Rn = 0.5, \quad N_t = 0.5,$$
$$F_0 = 0.1, \quad F_1 = 0.5, \quad We = 0.5, \quad G_r = 2.0, \quad m = 0.2, \quad Da = 0.2,$$
$$G_f = 1.0, \quad N_{TC} = 0.5, \quad G_c = 1.0, \quad M = 2.0, \quad N_b = 0.5, \quad d_2 = 1.0,$$
$$\beta = 0.5, \quad N_{CT} = 0.5, \quad l_1 = 0.1, \quad l_2 = 0.3, \quad l_3 = 0.5, \quad l_4 = 0.4.$$

5.1 Results Validation

Fig. 2 shows the validation of the present study's results by comparing them with the existing literature and numerical solutions for the peristaltic transport of a magnetized Williamson nanofluid in an asymmetric porous tapered channel under multiple slip conditions. The velocity profile in Fig. 2a shows that closely aligns with the findings of Bilal et al. [35], thus validating reliability and accuracy of the results. The temperature profile in Fig. 2b shows strong agreement with the presented results by Bilal et al. [35], thus validating reliability and accuracy of the present analysis. Furthermore, Fig. 2c shows a comparison between the analytical solution findings and the numerical solution obtained using the Bvp4c MATLAB solver, indicating a close agreement and verifying the correctness of the analytical approach. The strong similarity between the two results indicates that the perturbation-based analytical model used and presented in Python is robust and dependable. This successful validation further demonstrates the proposed methodology's ability to accurately characterize MHD Williamson nanofluid transport, underscoring its significance for biomedical applications, including nanoparticle-assisted drug delivery and hyperthermia therapy.

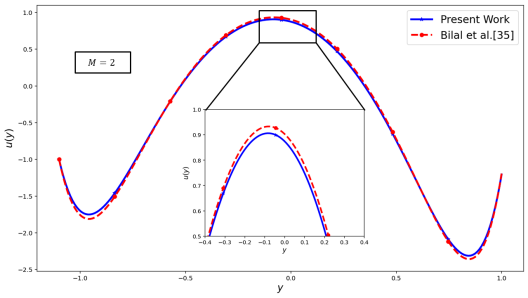

(a) Velocity Profile

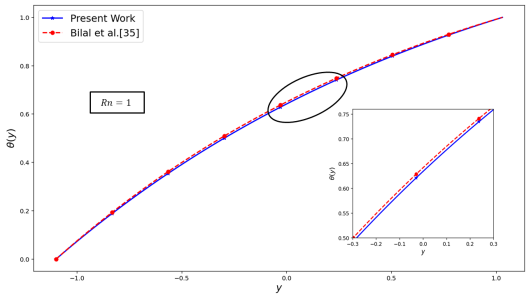

(b) Temperature Profile

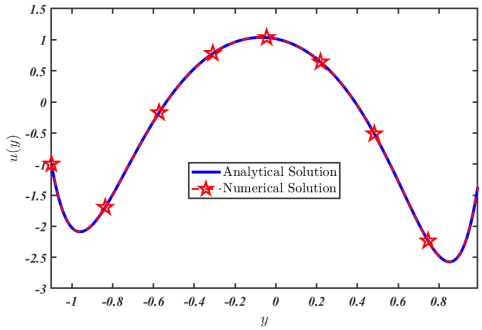

(c) Analytical Solution vs Numerical Solution

Figure 2: Comparison of the present velocity and temperature with the reference solution from Bilal et al. [35].

5.2 Velocity Profile

Fig. 3 shows the impact of Hartmann number ($M^2 = \frac{\sigma d^2 B_0^2}{\mu}$), Darcy number ($Da = \frac{k_0}{d^2}$), Weissenberg number ($We = \Gamma \frac{c}{\lambda}$), and nanoparticle Grashof number ($G_f = \frac{g(\rho_p - \rho_f)(\theta_1 - \theta_0)d^2}{\mu c}$) on the velocity distribution $u(y)$ for various parameter values. Fig. 3a shows that velocity variation with Hartmann number increases from $M = 1$ to $M = 4$. The velocity curves intersect at two distinct points: one at $(-0.66, -0.35)$ on the left side of the channel and the other at $(0.55, -0.45)$ on the right side. The interaction causes the Lorentz force, which opposes the motion of the fluid, to increase, leading to a decrease in the fluid's velocity. Fluid velocity decreases on both sides of the channel, but it increases in the center. Increased M enables better control of nanofluid velocity, essential for magnetically driven drug delivery, hyperthermia, and microfluidic flow control devices. However, after these points, the stronger magnetic field slows the velocity due to electromagnetic damping. The intersection points indicate where magnetic resistance equals natural flow acceleration. Fig. 3b shows that velocity variation with Darcy number increases from $Da = 0.1$ to $Da = 0.4$. The critical location of the left side of the velocity profiles intersects approximately at $(-0.566, -0.084)$ and on the right side at $(0.53, -0.553)$, where the influence of porous drag transitions to permeability-dominated flow behavior. The velocity reduces on both sides of the wall but increases in the resistance offered by the porous medium. Higher Da is related to transport through porous implants, biological tissues, and filtration systems where permeability significantly affects fluid penetration and drug transport. In contrast, beyond the intersection points, higher permeability (larger Da) facilitates smoother fluid motion, resulting in an acceleration of the flow. Thus, these intersection points indicate the equilibrium positions where the opposing effects of Darcy resistance and inertial acceleration balance each other. Fig. 3c shows the velocity distribution under viscoelastic effects for different Weissenberg number values $We = 0$ to $We = 0.2$. When increasing the Weissenberg number, it can increase the viscoelastic effect. It leads to reducing the velocity of the flow. The velocity intersects approximately on the left side $(-0.55, -0.015)$ and right side $(0.35, 0.087)$, indicating critical transition points in the flow behavior. An increasing We number exhibits stronger elastic characteristics in the central region of the channel and lies above the Newtonian case for higher We. This behavior reflects elastic stretching in the Williamson fluid, which enhances the velocity. In the Newtonian case, the higher viscoelastic effect can lead to a reduction in flow, which subsequently reduces the velocity near the walls. This is important for modeling blood flow, polymer-based drug carriers, and biofluids, as relaxation effects influence flow resistance and transport efficiency. Before these intersection points, the flow is predominantly governed by viscous (Newtonian-like) shear effects. So, the points where the lines cross show where the balance of power is changing between the resistance caused by shear and the acceleration caused by elasticity. Fig. 3d shows that the variation of velocity with the nanoparticle Grashof number values $G_f = 0.5$ to $G_f = 2.0$. The velocity profile at the critical transition point in the flow regime is represented by $(-0.931, -1.89)$ and $(0.33, 0.137)$. Stronger thermal buoyancy forces generated by the nanoparticles enhance the velocity when increasing the G_f number. In a newtonian fluid, the velocity profile is higher compared to non-Newtonian fluids. It represents the behavior of a purely viscous fluid. The velocity is low near the walls, contrasting at the center of the channel. Higher values improve heat and mass transfer, which is beneficial in nanomedicine, cooling of biomedical devices, and hyperthermia treatment. Thus, the points where the lines cross are where buoyancy-driven acceleration and viscous resistance change positions in the tapered channel.

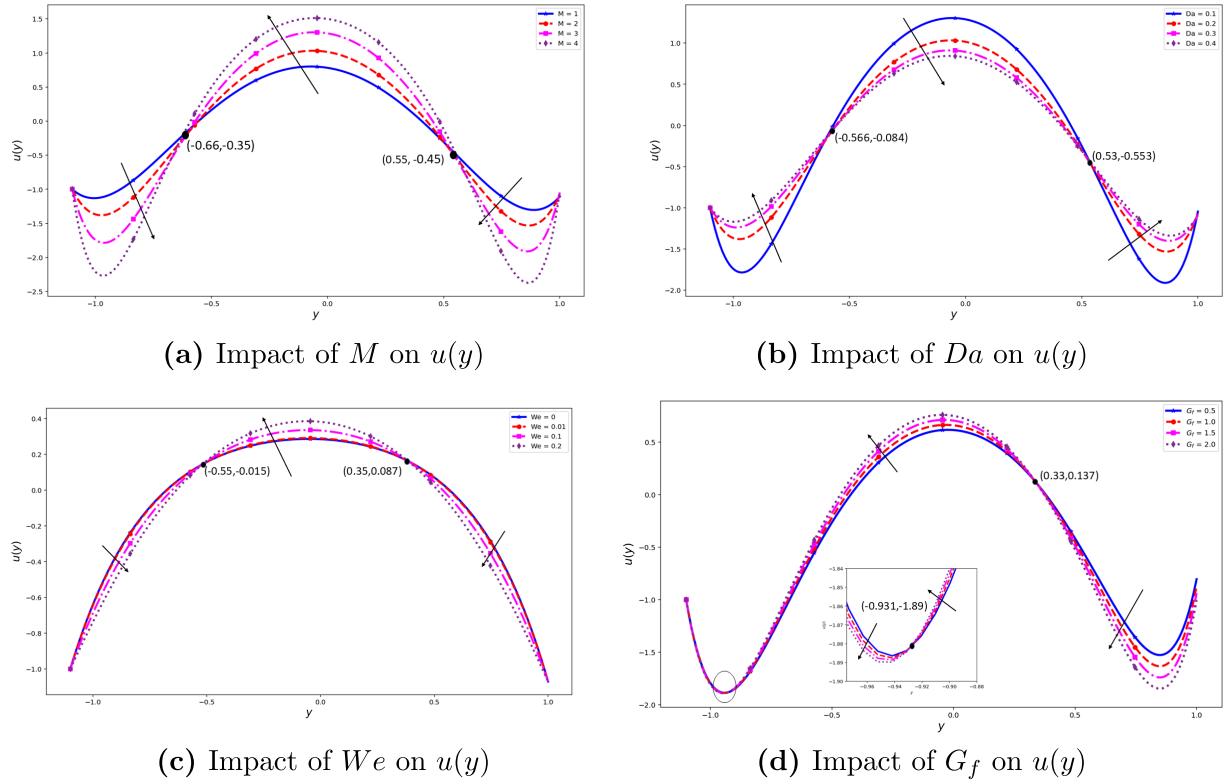

(a) Impact of M on $u(y)$ **(b)** Impact of Da on $u(y)$

(c) Impact of We on $u(y)$ **(d)** Impact of G_f on $u(y)$

Figure 3: Variation in the axial velocity distribution $u(y)$.

5.3 Temperature Profiles

Fig. 4 investigates the variation in temperature profile considering varying values of the thermal radiation parameter $(Rn = \frac{16\sigma^* T_0^3}{3\kappa^*(\mu c)_f})$, heat source/sink parameter $(\beta = \frac{Q_0 d_1^2}{(T_1 - T_0)\mu C_p})$, Brownian motion parameters $(N_b = \frac{\tau D_B(\Theta_1 - \Theta_0)}{\alpha_m})$, and Soret effects parameter $(N_{CT} = \frac{D_{CT}(T_1 - T_0)}{D_s(C_1 - C_0)}$. Fig. 4a shows the examination of the impact of the thermal radiation parameter (Rn) on the temperature profile $\theta(y)$. As (Rn) increases from $Rn = 1.0$ to $Rn = 4.0$, the temperature profile decreases throughout the asymmetric porous tapered channel. Higher radiation makes heat loss worse, thins the thermal boundary layer, and lowers the temperature of the fluid. As you go closer to the higher tapering wall, this impact gets stronger. Also, raising (Rn) makes the radiative cooling process in the Williamson nanofluid flow even stronger. Increasing Rn intensifies radiative heat transfer, leading to higher fluid temperature; this is important in thermal therapies and radiative heat management in biomedical systems. Fig. 4b investigates the change in the heat source/sink parameter β values, which increase from $\beta = 0.25$ to $\beta = 1.0$ on the temperature profile $\theta(y)$. When the temperature profile rises because of changes in the heat source and sink term. When β is positive, heat is generated inside the channel, consequent to an increase in temperature and a thickening of the thermal boundary layer. When hearing a sink, it reduces the temperature and steepens the thermal gradient. Therefore, whether heat is absorbed or released by the fluid is restrained by this parameter. Higher β enhances internal heat generation, raising the temperature field; this is relevant to metabolic heat generation and controlled thermal environments in biological tissues. Fig. 4c shows that impact of the Brownian motion parameter (N_b) changes the temperature distribution $\theta(y)$. As N_b increases, the temperature profile, from $N_b = 0.5$ to $N_b = 2.0$, can lead to a corresponding increase in the distribution. Physically, enhancing Brownian motion makes nanoparticles move more randomly, which increases the thermal diffusion in the fluid.

This higher nanoparticle activity helps move energy, which makes the thermal barrier layer thicker and raises the temperature across the asymmetric porous tapering channel. Improving thermal energy distribution; this supports enhanced heat transfer in nanomedicine and nanofluid cooling technologies. Fig. 4d shows the sway of the temperature curve $\theta(y)$ changes by changing the Soret effect (N_{CT}). As N_{CT} goes up from N_{CT} = 0.5 to N_{CT} = 2.0, the temperature gradient rises all the way along the channel. The temperature difference rises all the way across the channel. Increasing the number of nanoparticles in the fluid improves its thermal conductivity, which makes heat transfer easier. The interactions that happen inside the Williamson nanofluid channel make the thermal boundary layer bigger, which makes the temperature go up throughout the channel. Higher N_{CT} drives nanoparticles from hotter to colder regions, influencing temperature and concentration coupling; this is significant in targeted drug delivery and nanoparticle deposition in biomedical applications.

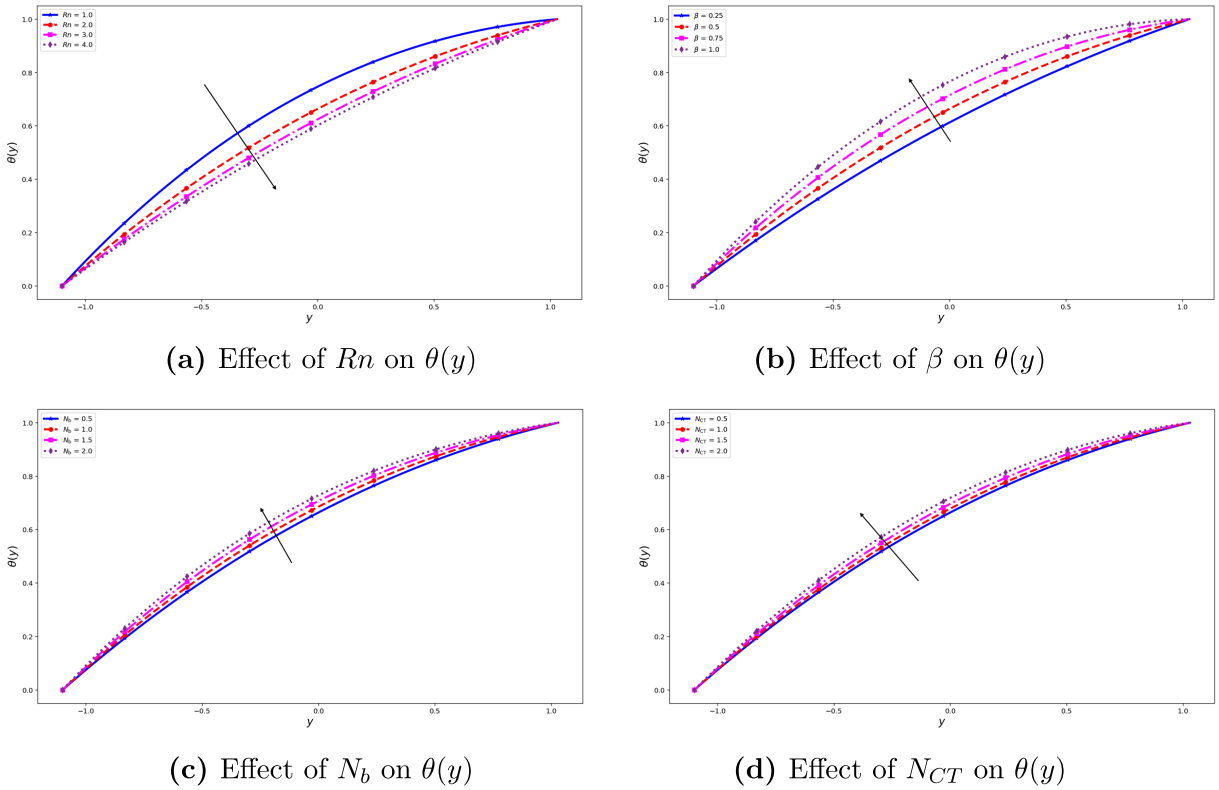

(a) Effect of Rn on $\theta(y)$ **(b)** Effect of β on $\theta(y)$

(c) Effect of N_b on $\theta(y)$ **(d)** Effect of N_{CT} on $\theta(y)$

Figure 4: Influence in the temperature distribution $\theta(y)$.

5.4 Concentration Profiles

Fig. 5 illustrates the variations in the solutal concentration $\sigma(y)$ and nanoparticle concentration $\gamma(y)$ for different values of Dufour effect parameters $(N_{TC} = \frac{\tau D_{TC}(C_1 - C_0)}{\alpha_m (T_1 - T_0)})$, Soret effect parameters (N_{CT}), Brownian motion parameters (N_b), and thermophoresis parameters $(N_t = \frac{\tau D_T (T_1 - T_0)}{T_0 \alpha_m})$. Fig. 5a illustrates the influence of the Dufour effect parameter $(N_{TC}$ = 0.5 to N_{TC} = 2.0) on the solutal concentration profile $\sigma(y)$. It is observed that the concentration decreases throughout the channel as N_{TC} increases. Physically, the concentration gradient caused by the Dufour effect in a mixture induces a heat flux, resulting in temperature changes. Modification of the temperature field by additional heat transfer strengthens and levels the coupling between thermal and solutal transport processes. As a result, reduced solute concentration

levels across the channel are thinner than the strengthened and level concentration boundary layers. This behavior highlights the significant role of cross-diffusion effects in regulating mass transfer in nanofluid flows. Higher N_{TC} represents influencing solutal distribution; this effect is relevant in coupled heat–mass transfer systems such as biomedical transport and microfluidic energy exchange devices. Fig. 5b shows the effect of the Soret parameter (N_{CT} = 0.5 to N_{CT} = 2.0) on the solutal concentration profile $\sigma(y)$. When increasing N_{CT} decreases the concentration across the channel. The Soret effect moves the particles from hotter to cooler regions because the effect induces mass flux due to the temperature gradient. This improved thermally induced diffusion moves the solute around in the fluid, which lowers the concentration levels near the channel. As a result, the concentration boundary barrier becomes thinner, which shows how closely linked heat and solutal transport mechanisms are in the nanofluid. Increasing N_{CT} enhances thermophoretic transport, causing nanoparticles/solute to migrate from hot to cold regions; this is important in targeted drug delivery, nanoparticle deposition, and thermal-driven separation processes.

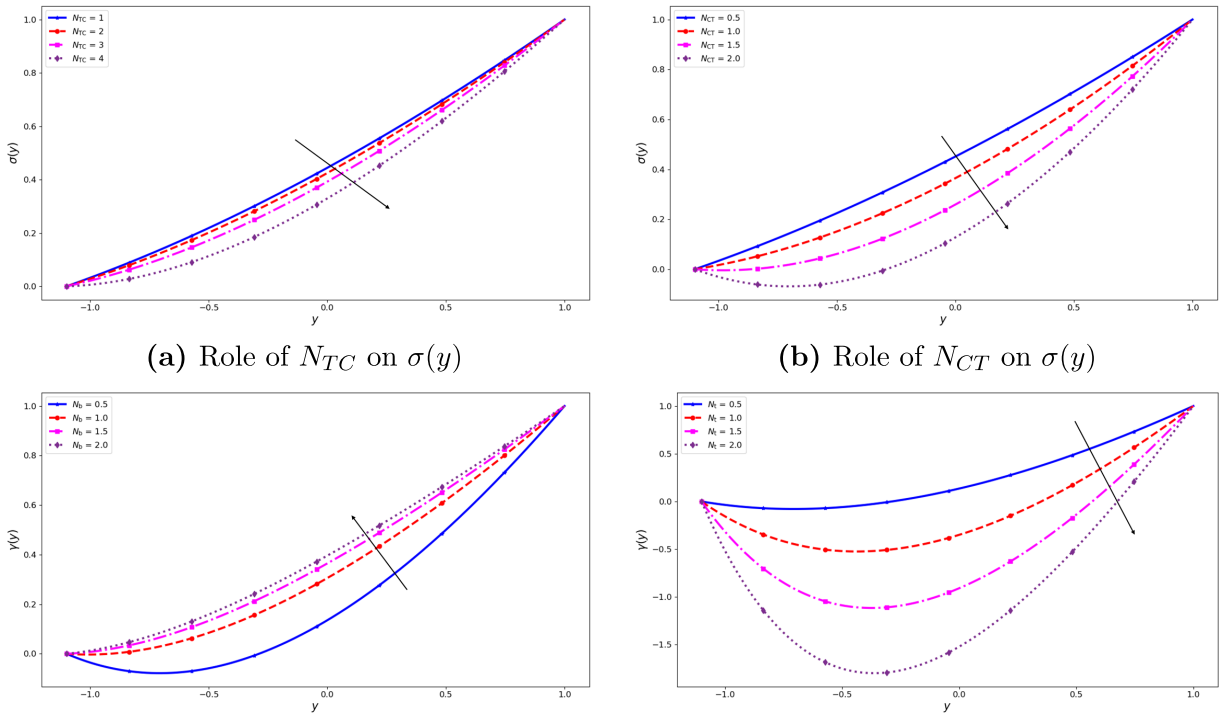

(a) Role of N_{TC} on $\sigma(y)$ **(b)** Role of N_{CT} on $\sigma(y)$

(c) Role of N_b on $\gamma(y)$ **(d)** Role of N_t on $\gamma(y)$

Figure 5: Variation in the solutal concentration $\sigma(y)$ and nanoparticle concentration $\gamma(y)$.

Fig. 5c shows the effect of Brownian motion (N_b = 0.5 to N_b = 2.0) on the nanoparticle concentration profile $\gamma(y)$ is analyzed. When $\gamma(y)$ increases, N_b simultaneously increases throughout the channel. Higher N_b can lead to random motion of nanoparticles, which enhances diffusive transport and promotes their redistribution within the fluid. This increased diffusion leads to a thicker concentration boundary layer and more uniform dispersion of nanoparticles across the channel. Consequently, enhancing the nanoparticle concentration level highlights the role of Brownian motion in governing nanoparticle distribution in nanofluid flows. Increasing N_b intensifies random nanoparticle motion, which enhances dispersion and alters concentration distribution; this is significant in nanomedicine, drug diffusion enhancement, and stabilization of nanofluids. Fig. 5d shows the variation of the nanoparticle concentration profiles $\gamma(y)$ with the thermophoresis parameter (N_t = 0.5 to N_t = 0.7) is analyzed. The analysis reveals that the concentration

of nanoparticles near the wall decreases as N_t increases. Thermophoresis moves nanoparticles from areas with higher temperatures to areas with lower temperatures, which causes them to move away from the heated wall. This enhances the concentration gradient and leads to a more non-uniform distribution across the channel. As a result, the concentration boundary layer becomes thinner along the wall. Higher N_t promotes migration of nanoparticles due to temperature gradients, modifying concentration boundary layers; this plays a key role in particle transport control, targeted therapies, and nanoparticle-based thermal systems.

5.5 Streamline Profiles

Fig. 6 analyzes how the Streamline profiles $\psi(y)$ for different values of the Hartmann number (M), Darcy number (Da), and Weissenberg number (We). This section examines appealing weakening outcomes and is especially useful in biomedical fields such as hyperthermia-based cancer treatment. Localized heating of viscous tissue is achieved by limiting fluid movement and reducing thermal risk in connecting healthy areas. The controlled flow around it also facilitates the delivery of nanoparticle-based medicinal agents to the correct site, improving treatment effectiveness and accuracy.

Fig. 6a illustrates the variations of magnetic parameters (M = 1 to 4) in streamlines are analyzed $\psi(y)$. Increasing the value of M can alter the flow structure by suppressing recirculation zones within the channel. A channel leads to a more streamlined and efficient flow pattern that enhances the overall transport properties of the Williamson nanofluid. Physically, higher M can strengthen the Lorentz force, which acts as a resistive body force opposing fluid motion and damping velocity fluctuations. Results: the streamlines become smoother and more uniformly distributed, indicating diminished secondary flow intensity. When M is smaller, strong oscillations and isolated eddies are seen because the electromagnetic effects are weaker. When M is larger, the flow becomes steadier and more structured, and the Williamson nanofluid starts to seem more like a single direction. Fig. 6b analyzes the impact of Darcy numbers from Da = 0.1 to Da = 0.4 based on the streamline patterns. As the Darcy number (Da) decreases, the permeability of the porous medium also decreases, leading to increased resistance to flow due to heightened drag within the porous matrix. As Da increases, simultaneously, the porous medium exhibits higher permeability. This process diminishes the porous resistance and facilitates the fluid's movement through the channel. Consequently, the streamlines become more uniformly distributed and less distorted, while recirculation regions diminish. This transition reflects enhanced flow transport and a tendency toward more streamlined, unidirectional motion in highly permeable porous configurations. Fig. 6c investigates the influence of the Weissenberg number $We = 0, 0.02, 0.1, 0.3$ on the streamline flow patterns. At lower Weissenberg numbers, the fluid exhibits Newtonian behavior, resulting in smooth and uniformly spaced streamlines. As the higher We number acts as non-Newtonian behavior, resulting in more viscoelastic effects, this effect can retain fluid relaxation time. These viscoelastic effects introduce normal stress differences and energy storage within the fluid, which distort the streamline structure and promote the formation of closed-loop recirculation cells. Consequently, the flow becomes more complex and less stable, reflecting the increasing dominance of elastic forces over viscous effects in the Williamson nanofluid.

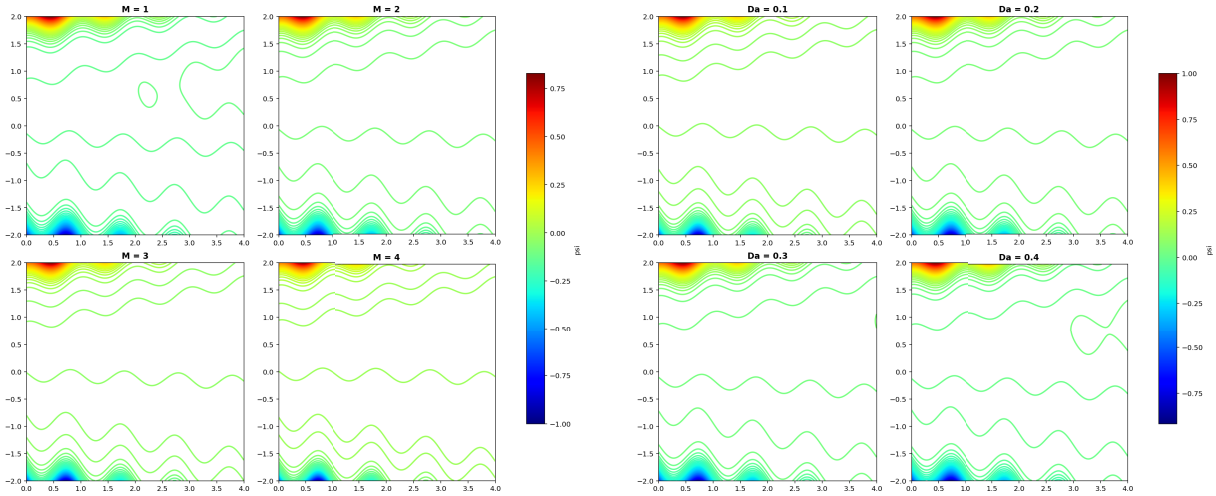

(a) Effect of M on $\psi(y)$

(b) Effect of Da on $\psi(y)$

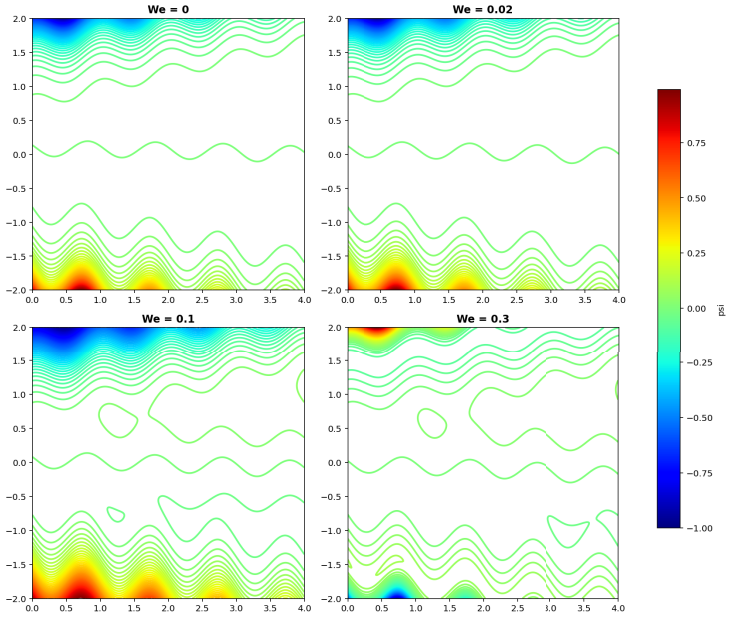

(c) Effect of We on $\psi(y)$

Figure 6: Influence of stream function filed $\psi(y)$.

5.6 Pressure Drop

The instantaneous flow rate $F(x,t)$ is introduced to characterize the transient features of the peristaltic motion through the phase variable $(x-t)$. It is expressed as

$$F(x,t) = Q + d_1 + mx + a_1 \sin(2\pi(x-t)+\phi) - d_2 - mx \sin(2\pi(x-t)). \tag{66}$$

Fig. 7 illustrates how this flow rate behaves when a Williamson fluid undergoes peristaltic transport. The mean pressure rise Δp is evaluated numerically using simulations performed in Mathematica and Python. The results highlight the role of key parameters such as the non-dimensional wall amplitudes (a_1, a_2),

the Hartmann number M, and the Weissenberg number We on the pressure rise Δp. These variations demonstrate the sensitivity of the peristaltic pumping mechanism to changes in channel geometry, magnetic effects, and fluid elasticity.

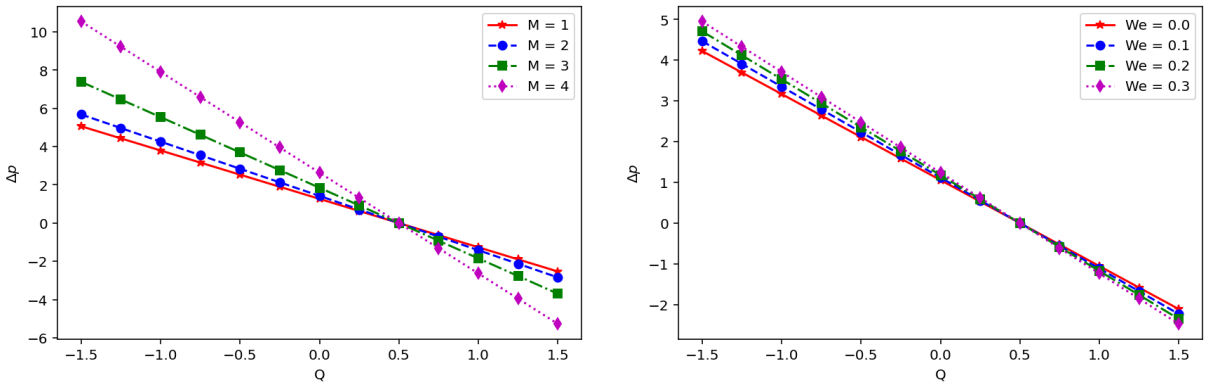

(a) Effect of M on Δp **(b)** Effect of We on Δp

Figure 7: Impact of the pressure drop Δp with the Hartmann number M & Weissenberg number We.

Fig. 7a shows that the pressure drop Δp decreases in an approximately linear manner with an increasing volumetric flow rate Q. This signifies a smooth transition between the pumping and co-pumping regions; this transition is governed by the balance between pressure forces and fluid transport. As the Hartmann number $(M = 1 \text{ to } M = 4)$ increases, the Lorentz force intensifies and opposes the flow, thereby increasing hydrodynamic resistance. Consequently, a larger pressure rise is required in the negative Q region, while a larger pressure drop is observed in the positive Q region. This behavior reflects the damping effect of the magnetic field on the conducting Williamson nanofluid. It decreases the velocity and demands a larger pressure drop to sustain the flow within the porous conical channel. Fig. 7b demonstrates that the volumetric flow rate (Q) increases as the pressure drop (Δp) decreases. This signifies the existence of a consistent equilibrium between the applied pressure drop and fluid transport. As the Weissenberg number $We = 0$ to $We = 0.3$ increase; a slight rise in Δp is observed in the negative Q regime; this is attributed to increased elastic resistance resulting from fluid memory effects. Physically, a higher We corresponds to an increased relaxation time, which intensifies elastic stresses and resists deformation. Conversely, for positive Q, an increase in We results in an additional pressure drop. This occurs because the viscoelastic fluid exhibits enhanced stretching and alignment in the direction of flow, thereby reducing resistance. Although this effect is moderate, it remains consistent across the entire range of Q. This evidence suggests that viscoelastic stresses progressively modify the pressure requirements for nanofluid transport within the channel.

Pressure Gradient:

Fig. 8 analyzes how the axial pressure gradient changes along the axial coordinate $(\frac{dp}{dx})$ for different values of the Darcy number (Da) and Thermal Grashof number $(G_r = \frac{gd^2\rho_f\beta_T(1-\theta_0)(T_1-T_0)}{\mu c})$. Fig. 8a illustrates that the pressure gradient $(\frac{dp}{dx})$ decreases as the Darcy number from $(Da = 0.1 \text{ to } Da = 0.4)$ increases. This indicates that the resistance to flow within the porous medium is reduced. Physically, a higher Darcy number signifies greater permeability; this effect diminishes the drag exerted by the porous structure, thereby facilitating fluid flow. Consequently, a diminished pressure gradient is necessary to maintain the flow. The roughly linear decline observed in the curves suggests improved axial transport, and the decrease in oscillation amplitude points to more uniform pressure fluctuations along the channel's length. This attribute corroborates the crucial role of permeability in reducing hydrodynamic resistance and facilitating fluid

transport within the porous tapered channel. Fig. 8b shows that the pressure gradient $\frac{dp}{dx}$ increases as the thermal Grashof number values for (G_r = 0.1 to G_r = 0.4) increase, indicating a reduction in the required driving pressure. Physically, the Grashof number represents the ratio of buoyancy forces to viscous forces; consequently, a higher value of G_r implies stronger thermal buoyancy forces, which facilitate the axial motion of the fluid. Consequently, pressure resistance decreases, and the streamlines inside the channel ascend. The overall amplitude of the pressure distribution diminishes due to the upward influence of temperature gradients, yet its rhythmic nature remains unchanged. This confirms that buoyant forces are crucial for sustaining flow by reducing the external pressure required for movement through the channel.

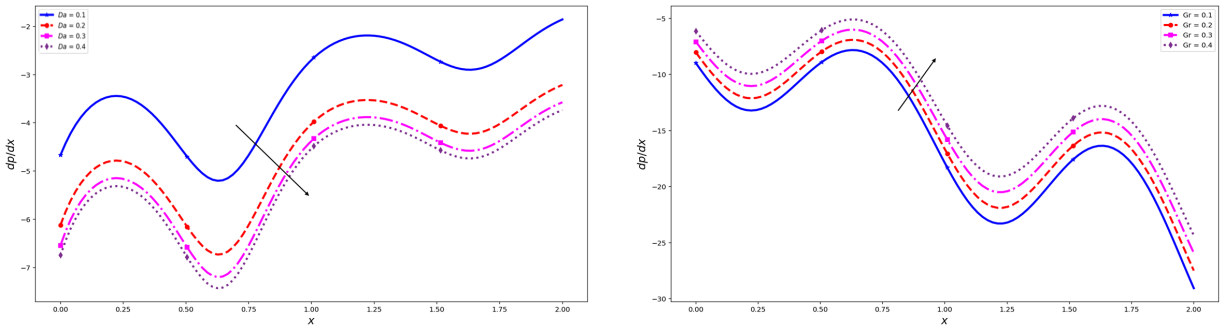

(a) Effect of Da on $\frac{dp}{dx}$ **(b)** Effect of G_r on $\frac{dp}{dx}$

Figure 8: Variation of the pressure gradient $\frac{dp}{dx}$ with Darcy number Da and Grashof number G_r.

5.7 Skin Friction (τ_w)

Fig. 9 shows the effect of Hartmann number (M) and Darcy number (Da) on the skin friction profile in relation to the axial coordinate for varying parameter values. Fig. 9a shows that the Hartmann number (M = 0.5 to M = 2.0) increases, and the surface friction τ_w also increases; this indicates that the wall shear stress resulting from magnetic effects has intensified. An increasing M can strengthen the Lorentz force, which can slow down the flow in the channel. This slowdown creates steeper velocity changes near the walls, which then increases the shear stress at the boundaries. The stronger magnetic damping helps dissipate momentum, effectively making the fluid layers near the walls more resistant to motion. Furthermore, the growing difference between the upper and lower τ_w values indicates that magnetic forces significantly change the shear distribution, especially in an asymmetric channel. Fig. 9b illustrates the variation of the wall shear stress τ_w with the Darcy number (Da = 0.2 to Da = 0.5). As the Darcy number (Da) increases, a notable decrease in τ_w is observed, which signifies a reduction in wall resistance. Physically, a larger Darcy number suggests enhanced permeability; this, in turn, diminishes the drag force imposed by the porous medium, facilitating a more effortless fluid flow through the channel. Consequently, this decrease in porous resistance fosters a more uniform velocity distribution in the vicinity of the walls, which results in smaller velocity gradients and, therefore, a reduction in shear stress. The observed decrease in τ_w on both the upper and lower walls is indicative of the diminished momentum dissipation and reduced drag experienced within highly permeable porous media.

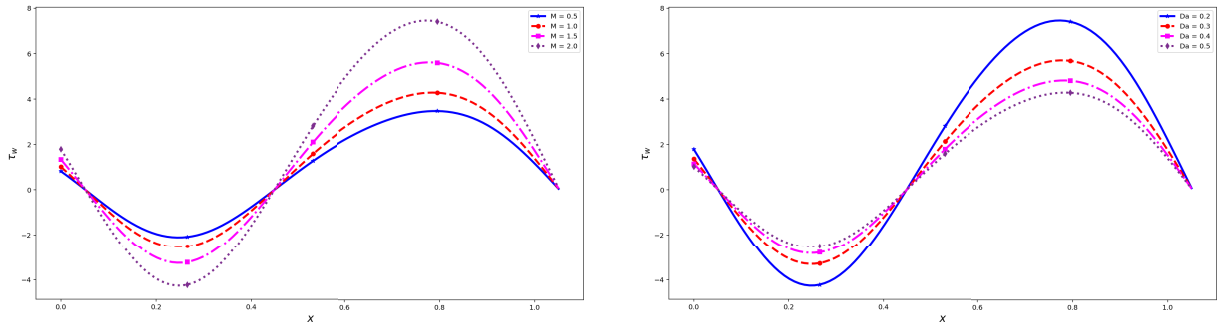

(a) Effect of M on τ_w **(b)** Effect of Da on τ_w

Figure 9: Variation of the skin friction τ_w with the Hartmann number M and Darcy number Da.

5.8 Nusselt Number (Nu)

Fig. 10 illustrates the influence of the Nusselt number (Nu) varies with different values of the heat source/sink parameter (β) and Brownian motion parameter (N_b). Fig. 10a shows the examined influence of the heat source/sink parameter for $\beta = 0.25$ to 1.0 on the Nusselt number. An increase in β enhances the Nusselt number and can improve heat transfer near the channel walls. Consequently, the convective heat transfer rate increases, leading to a higher peak in the Nusselt number distribution. Conversely, as the values of β increase, the negative regions of the curve become more pronounced, indicating intensified heat absorption during the cooling phase of the peristaltic cycle. The heat source/sink parameter changes the thermal field, affecting how quickly the flow area heats up and cools down. Fig. 10b illustrates that the Nusselt number decreases by increasing the Brownian motion parameter $(N_b = 0.5$ to $N_b = 2.0)$, which leads to reduced heat transfer at the wall. Higher N_b intensifies the random motion of nanoparticles, which enhances the dispersion of thermal energy within the fluid and thickens the thermal boundary layer. Consequently, the Nusselt number decreases throughout the peristaltic cycle. This changes Brownian diffusion in attenuating heat transfer at the wall, despite the increased redistribution of internal energy within the nanofluid.

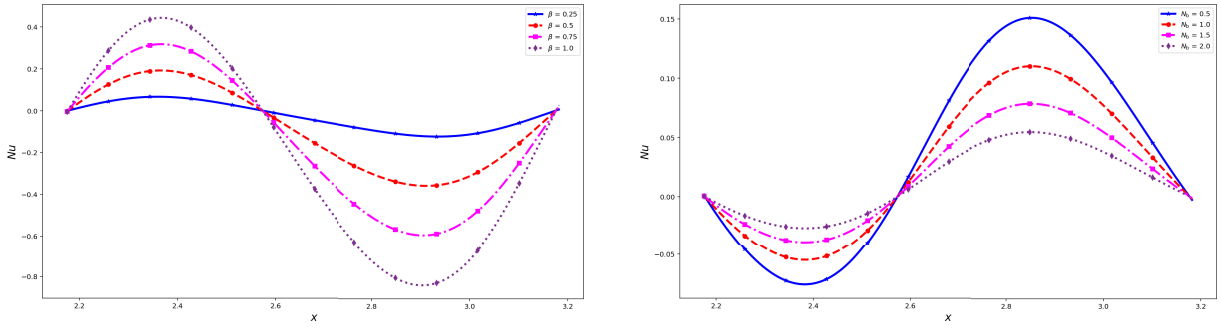

(a) Effect of β on Nu **(b)** Effect of N_b on Nu

Figure 10: Variation of the Nusselt number Nu with the heat source parameter β and Brownian motion parameter N_b.

5.9 Sherwood Number (Sh)

Fig. 11 investigates how the Sherwood number distribution (Sh) changes along the axial coordinate for different values of the thermal radiation parameter (Rn) and Soret effects parameter (N_{CT}). Fig. 11a shows that as the thermal radiation parameter $(Rn = 1$ to $Rn = 4)$ increases, the Sherwood number decreases; this indicates a reduction in mass transfer at the wall. Physically, strong thermal radiation elevates the fluid

temperature, which, through associated thermo-solutal effects, alters the concentration field. Consequently, concentration gradients near the walls reduce, leading to a reduction in mass flux. As a result, the Sherwood number curves decline with increasing Rn (the ratio of buoyancy forces to viscous forces), signifying a decrease in mass transfer rates. This trend indicates that thermal radiation indirectly inhibits species diffusion by altering the configuration of the concentration boundary layer. Fig. 11b shows the effect of the Soret parameter (N_{CT} = 0.5 to N_{CT} = 3.5) on the Sherwood number (Sh). It is observed that Sh increases significantly as N_{CT} increases, indicating an enhancement in mass transfer at the wall. Physically, the Soret effect (thermo-diffusion) drives the transport of species from regions of higher temperature to regions of lower temperature, thereby intensifying concentration gradients near the channel walls. This steep gradient augments the mass flux, leading to higher values of the Sherwood number. Consequently, as N_{CT} increases, the Sh profiles shift upward, and the peak values become more pronounced throughout the peristaltic cycle. This oscillatory behavior mirrors the underlying peristaltic motion, while the upward trend confirms that stronger thermo-diffusion effects promote mass transfer within the nanofluid.

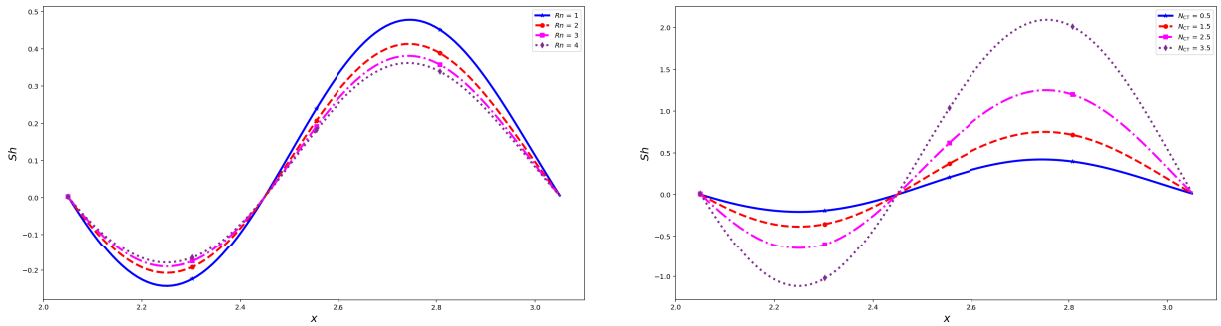

(a) Effect of Rn on Sh **(b)** Effect of N_{CT} on Sh

Figure 11: Variation of the Sherwood number Sh with the thermal radiation parameter Rn and the Soret parameter N_{CT}.

6 Machine Learning Approach

Machine learning is integrated with the perturbation method to predict the MHD flow of Williamson nanofluid in an asymmetric porous tapering channel. The input physical parameters M, Da, We, Rn, β, N_b, N_t, N_{CT}, N_{TC}, l_1, l_2, l_3, and l_4 are used to estimate the skin friction coefficient τ_w, Nusselt number (Nu), and Sherwood number (Sh) using supervised machine learning algorithms, including Linear Regression (LRG), Logistic Regression (LR), Naive Bayes (NB), Support Vector Machines (SVM), Decision Trees (DT), Random Forests (RF), and Artificial Neural Networks (ANN). The dataset of 500 observations each is obtained from analytical solutions, scaled, and divided into 70% training and 30% testing subsets. Model efficiency is evaluated through a confusion matrix and statistical measures, including accuracy, precision, recall, and F1-score, along with regression metrics such as Mean Squared Error (MSE), Root Mean Squared Error $(RMSE)$, and Mean Absolute Error (MAE). This hybrid framework improves predictive assessment of nanofluid transport behavior.

Figs. 12–14 show that confusion matrices of various supervised machine learning models are used to predict the Nusselt number (Nu), Sherwood number (Sh), and skin friction coefficient (τ_w). Figs. 15–17 illustrate that the error metrics of different supervised machine learning models for predicting the Nusselt number (Nu), Sherwood number (Sh), and skin friction coefficient (τ_w) highlight variations in model accuracy and validity. Tables 1 and 2 investigate the classification performance of various supervised machine learning models for Nusselt number (Nu), Sherwood number (Sh), and skin friction coefficient (τ_w),

demonstrating that ensemble models obtain the highest calculation accuracy (%), precision, recall, F1-score, MAE, MSE, and RMSE.

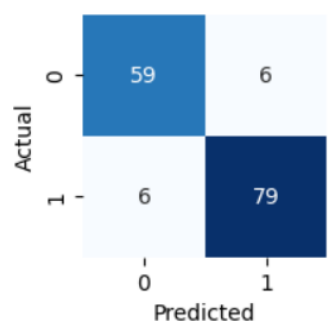

(a) Linear Regression

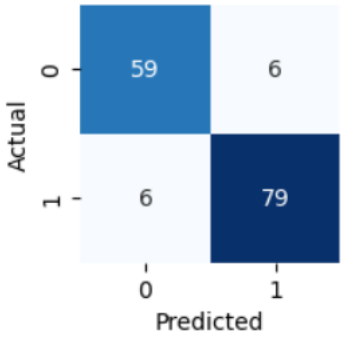

(b) Logistics Regression

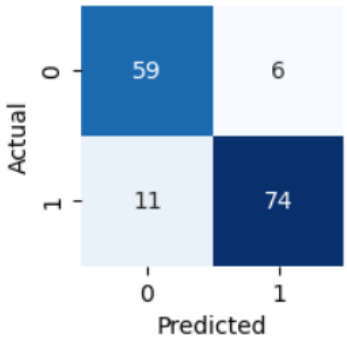

(c) Support Vector Machines

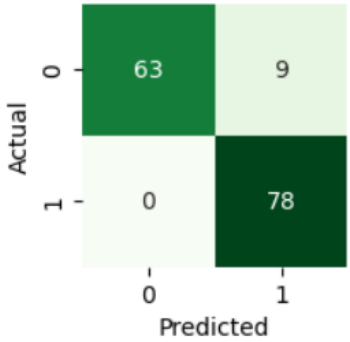

(d) Naive Bayes

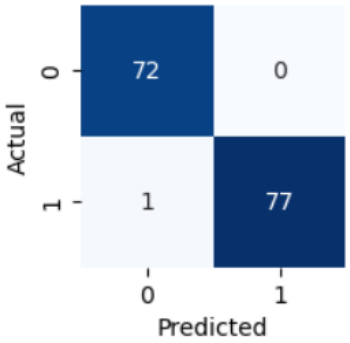

(e) Decision Trees

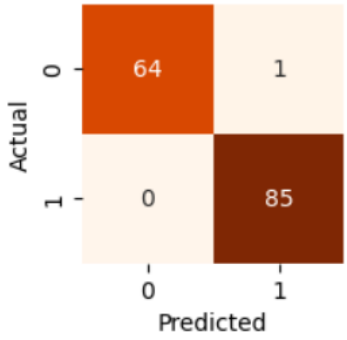

(f) Random Forests

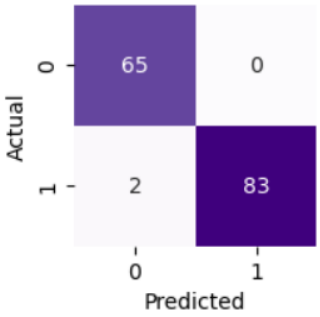

(g) Artificial Neural Network

Figure 12: Determine the model's confusion matrix for the Nusselt number.

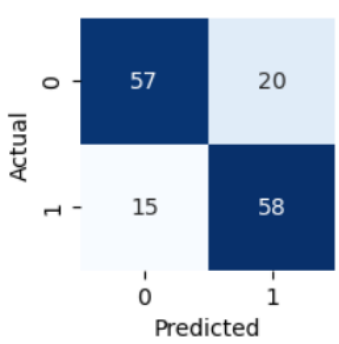

(a) Linear Regression

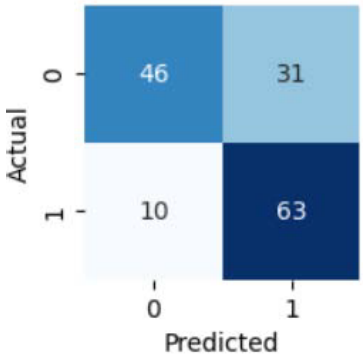

(b) Logistics Regression

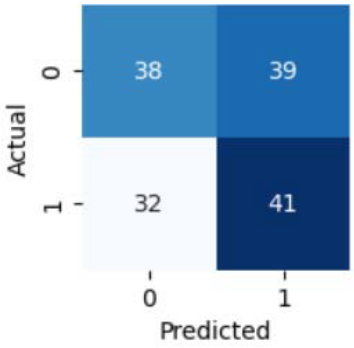

(c) Support Vector Machines

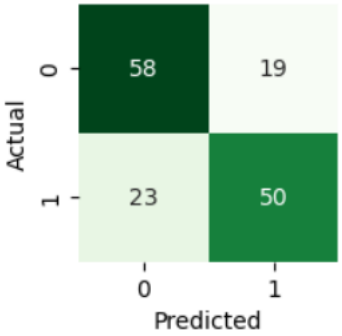

(d) Naive Bayes

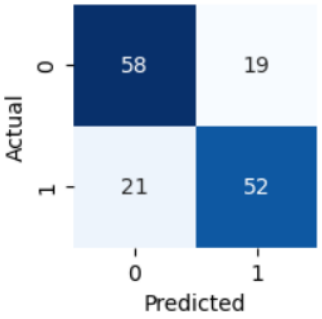

(e) Decision Trees

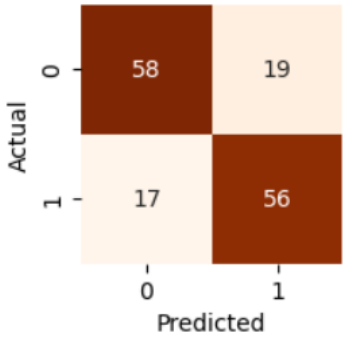

(f) Random Forests

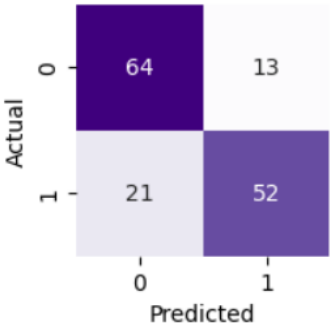

(g) Artificial Neural Network

Figure 13: Determine the model's confusion matrix for the Sherwood number.

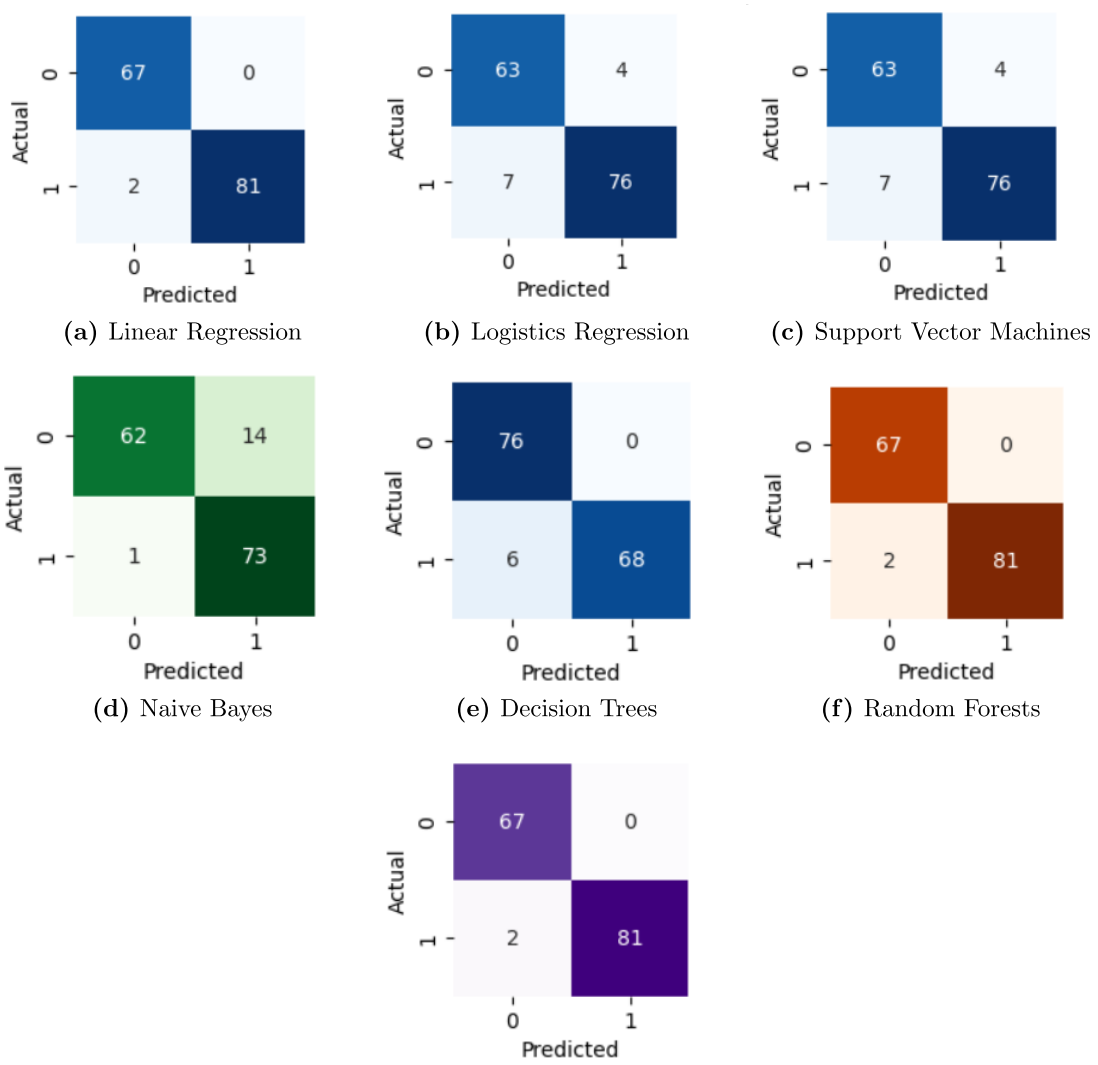

(a) Linear Regression (b) Logistics Regression (c) Support Vector Machines

(d) Naive Bayes (e) Decision Trees (f) Random Forests

(g) Artificial Neural Network

Figure 14: Determine the model's confusion matrix for the skin friction (τ_w).

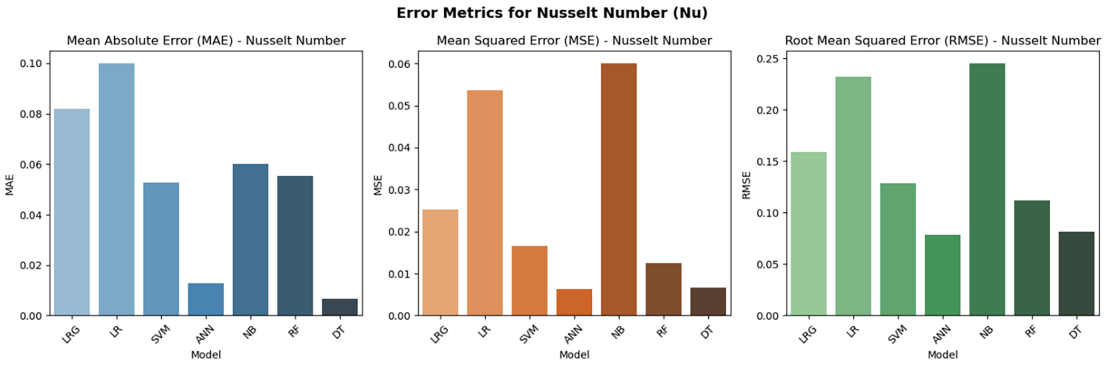

Figure 15: Error for Nusselt number.

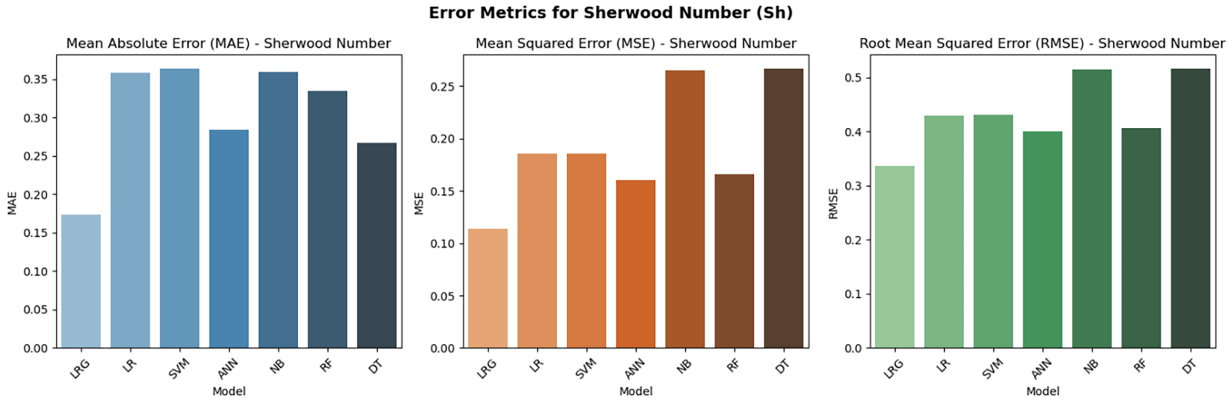

Figure 16: Error for Sherwood number.

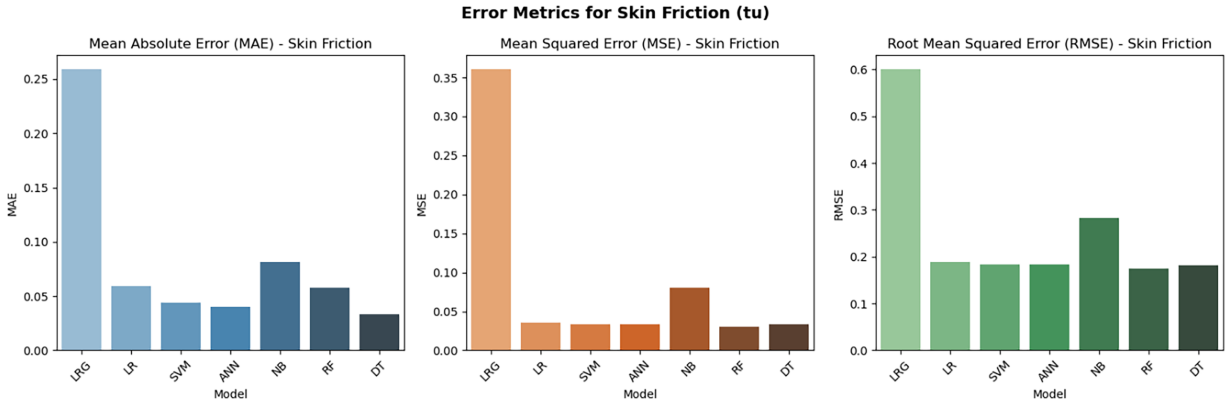

Figure 17: Error for skin friction.

Table 1: Classification metrics summary for Nusselt number (Nu), Sherwood number (Sh), and skin friction coefficient (τ_w)

Model	Parameter	Accuracy (%)	Precision	Recall	F1-Score
LRG	Nu	92.00	0.93	0.93	0.93
	Sh	89.10	0.82	0.88	0.86
	τ_w	98.70	1.00	0.98	0.99
LR	Nu	92.00	0.93	0.93	0.93
	Sh	88.00	0.83	0.86	0.80
	τ_w	92.7	0.95	0.92	0.93
NB	Nu	94.00	0.90	1.00	0.95
	Sh	88.95	0.87	0.90	0.89
	τ_w	90.00	0.98	0.99	0.91
DT	Nu	99.3	1.00	0.99	0.99
	Sh	89.50	0.83	0.81	0.82
	τ_w	96.00	1.00	0.92	0.96

(Continued)

Table 1 (continued)

Model	Parameter	Accuracy (%)	Precision	Recall	F1-Score
RF	Nu	99.30	0.99	1.00	0.99
	Sh	86.00	0.85	0.88	0.86
	τ_w	98.70	1.00	0.98	0.99
SVM	Nu	88.70	0.93	0.87	0.90
	Sh	84.00	0.81	0.88	0.80
	τ_w	92.70	0.95	0.92	0.93
ANN	Nu	98.70	1.00	0.98	0.99
	Sh	87.3	0.80	0.81	0.85
	τ_w	98.70	1.00	0.98	0.99

Table 2: Error metrics summary (MAE, MSE, RMSE) for Nusselt number (Nu), Sherwood number (Sh), and skin friction coefficient (τ_w)

Model	Parameter	MAE	MSE	RMSE
LRG	Nu	0.0819	0.0252	0.1588
	Sh	0.1735	0.1137	0.3372
	τ_w	0.2590	0.3605	0.6004
LR	Nu	0.0999	0.0537	0.2317
	Sh	0.3582	0.1853	0.4304
	τ_w	0.0594	0.0355	0.1884
NB	Nu	0.0600	0.0600	0.0600
	Sh	0.3599	0.2654	0.5152
	τ_w	0.0818	0.0805	0.2837
DT	Nu	0.0067	0.0061	0.0816
	Sh	0.2667	0.2661	0.5164
	τ_w	0.0333	0.0333	0.1826
RF	Nu	0.0553	0.0125	0.1119
	Sh	0.3343	0.1658	0.4072
	τ_w	0.0575	0.0305	0.1747
SVM	Nu	0.0526	0.0165	0.1283
	Sh	0.3634	0.1855	0.4307
	τ_w	0.0441	0.0335	0.1831
ANN	Nu	0.0127	0.0062	0.0786
	Sh	0.2846	0.1601	0.4001
	τ_w	0.0399	0.0340	0.1845

1. **Linear Regression (LRG):**
The linear regression model shows high classification accuracy for the Nusselt number (Nu) and skin friction coefficient (τ_w) with values of 92.00% and 98.70%, respectively, whereas the accuracy for the Sherwood number (Sh) is comparatively lower at 89.10%. Precision, recall, and F1-scores remain high, indicating stable classification performance. However, the regression error metrics reveal notable limitations, particularly for τ_w, where the RMSE reaches 0.6004 and the MAE is 0.2590. These elevated errors suggest that LRG is unable to adequately capture the nonlinear shear and transport characteristics inherent in tapered porous channel flows.
2. **Logistic Regression (LR):**
The logistic regression demonstrates strong predictive performance across all parameters, achieving accuracies of 88.00% for Sh, 92.70% for τ_w, and 92.00% for Nu. The model exhibits excellent recall for Nu, which is 0.93, and high precision for τ_w, which is 0.95, supported by strong F1-scores, particularly for Nu and τ_w, which is 0.93. Regression analysis further supports this performance with relatively low RMSE values of 0.1884 for τ_w and 0.2317 for Nu. These results indicate that LR performs well in classification tasks but has some limitations in fully capturing strong nonlinear coupling effects in thermo-fluid transport.
3. **Naive Bayes (NB):**
The Naive Bayes classifier provides reasonable predictions for Nu with an accuracy of 94.00%, and stable precision is 0.90, recall is 1.00, and F1-score is 0.95. However, its performance declines for the Sh and τ_w, as reflected by comparatively lower F1-scores and increased error metrics. In particular, RMSE values for Sh are 0.5152, and τ_w is 0.2837, indicating low predictive accuracy. This behavior suggests that the Naive Bayes model struggles to effectively account for the complex interdependencies among heat-fluid parameters, thereby limiting its overall reliability regarding these associated variables.
4. **Decision Tree (DT):**
The decision tree model shows strong predictive capability with accuracies of 96.00% for τ_w, 99.30% for Nu, and 89.50% for Sh. The model demonstrates strong classification capability, with precision and recall values reaching up to 1.00 and 0.99, respectively, particularly for Nu. Furthermore, relatively low RMSE values of 0.0816 for Nu and 0.1826 for τ_w indicate its effectiveness in capturing nonlinear variations in the flow system. Although slightly lower performance is observed for Sh, the decision tree remains a reliable and interpretable model for analyzing transport phenomena in porous channels.
5. **Random Forest (RF):**
Random Forest achieves consistently high accuracies of 98.70% for τ_w, 99.30% for Nu, and 86.00% for Sh. It maintains a good balance between precision and recall, both reaching values close to 1.00 for Nu and τ_w. The ensemble nature of RF helps reduce prediction errors, as reflected by lower RMSE values of 0.1119 for Nu and 0.1747 for τ_w, although slightly higher error (0.4072) is observed for Sh. These results confirm RF's ability to effectively model multiscale nonlinear relations in Williamson nanofluid transport.
6. **Support Vector Machine (SVM):**
The Support Vector Machine model shows moderate to good predictive capability, with accuracies of 88.70% for Nu, 84.00% for Sh, and 92.70% for τ_w. It achieves strong precision values (up to 0.95) and balanced recall, indicating stable classification performance. Although RMSE values are relatively higher for Sh at 0.4307 and τ_w at 0.1831, this indicates that there are certain limitations in detecting complex non-linearities. However, the kernel-based framework allows for a reasonable estimation of the transport dynamics within the system using SVM.

7. **Artificial Neural Network (ANN):**
   The Artificial Neural Network provides consistent and reliable performance with accuracies of 98.70% for both Nu and τ_w, and 87.30% for Sh. High precision and recall values in the range 1.00 to 0.98 lead to strong F1-scores, indicating reliable predictions. Additionally, low RMSE values, particularly of 0.0786 for Nu and 0.1845 for τ_w, highlight its superior capability in capturing nonlinear behavior. Although performance for Sh is slightly lower, the ANN effectively models the coupled heat and mass transfer processes, making it a highly suitable approach for thermo-fluid analysis in tapered porous channels.

7 Conclusion

The present study examines the flow behavior of a Williamson nanofluid in an asymmetric, porous, tapered, and inclined channel under the combined effects of a magnetic field, thermal radiation, porous medium resistance, buoyancy forces, and internal heat generation or absorption, while also incorporating multi-slip boundary conditions to realistically represent wall–fluid interactions. The governing equations of this model are transformed into dimensionless form and solved analytically using a perturbation technique. The influence of physical parameters on heat and mass transfer characteristics is systematically analyzed. Furthermore, a soft computing approach, namely the Supervised Machine Learning (SML) technique, is employed to predict important transport quantities such as the Nusselt number, skin friction, and Sherwood number. Finally compare the results to ensure the accuracy level of drug delivery.

- An increase in the Hartmann number (M) reduces velocity due to the Lorentz force, which increases surface friction and pumping pressure. Conversely, a higher Darcy number (Da) reduces pore resistance, allowing for smoother flow and decreasing both the pressure gradient and shear stress at the wall.
- The Weissenberg number (We) improves the viscoelastic behavior of the fluid, increasing velocity and modifying the streamline pattern. Furthermore, the buoyancy parameters (G_f and G_r) accelerate fluid movement and reduce the negative pressure gradient, favoring peristaltic transport.
- Thermal radiation (Rn) reduces the thickness of the thermal boundary layer and tends to cool the fluid, while the heat source/sink parameter (β) increases the temperature and internal energy in the flow field.
- The Brownian motion parameter (N_b) increases nanoparticle diffusion, raising both temperature and concentration, while simultaneously reducing the heat transfer rate (Nu). The thermophoresis parameter (N_t) drives nanoparticles from warmer to cooler regions, resulting in greater nanoparticle accumulation near the channel wall.
- The Soret parameter (N_{CT}) intensifies mass transport due to temperature gradients, while the Dufour parameter (N_{TC}) promotes heat transfer due to concentration gradients. Consequently, heat and mass transfer rates (Nu and Sh), as well as surface friction (τ_w), are strongly influenced by magnetic, thermal, and nanoparticle parameters, allowing for better control of transport processes in biomedical applications.
- An integrated perturbation method and machine-learning framework effectively simulated Williamson nanofluid flow in an asymmetric porous tapered channel under different slip conditions.
- Linear and probabilistic models such as Linear Regression (LRG), Logistic Regression (LR), and Naive Bayes (NB) provide acceptable predictions, particularly for Nu, but show comparatively higher error metrics and lower performance for Sh and τ_w, indicating limitations in handling strongly nonlinear and coupled thermofluid behavior.
- Tree-based models demonstrate strong predictive capabilities. The Decision Tree (DT) achieves very high accuracy for Nu (99.30%) and τ_w (96.00%) with low RMSE values; meanwhile, the Random Forest (RF) further enhances both stability and accuracy, attaining 99.30% for Nu and 98.70% for τ_w.

Furthermore, error metrics are reduced, thereby validating the effectiveness of ensemble learning in understanding nonlinear transport phenomena.

- The Support Vector Machine (SVM) model delivers reliable classification performance specifically for τ_w characterized by balanced precision and recall; however, slightly higher RMSE values for Sh and Nu indicate a minor limitation in regression accuracy.
- Artificial Neural Networks (ANN) provide very reliable and resilient performance. They achieve an accuracy of 98.70% for the Nu and τ_w values, accompanied by low RMSE values. Their capacity to consider the intricate nonlinear connections between heat transport, mass diffusion, and shear stress makes them exceptionally appropriate for advanced thermal-fluid and biological applications.

Future Scope

Future work can enhance 3-dimensional flow analysis. Certain hybrid nanofluids provide more accurate modeling of complex fluids. This research can also explore non-uniform magnetic fields, entropy generation, time-dependent flow systems, and machine learning models, including the AI in Computational Fluid Dynamics algorithm, deep learning, and hybrid optimization techniques like Physics-Informed Neural Networks (PINNs), to analyze the complexity and nonlinearity of Williamson nanofluid flow and peristaltic transport.

Acknowledgement: The authors would like to express their sincere gratitude to SRM Institute of Science and Technology for providing the facilities and support for this research work.

Funding Statement: The authors declare that no specific funding was received for the conduct of this research.

Author Contributions: H. Kamlesh: Conceptualization of research problem, developing the research idea, mathematical formulation, objectives, writing an initial draft, perturbation solution, supervised machine learning models, designing solution methods, coding algorithms, interpreting trends, designing graphs; E. P. Siva: Mathematical formulation, physical model, supervising, reviewing, technical review and editing; P. Bathmanaban: Developing the research idea, mathematical formulation; O. D. Makinde: Review and editing, improving geometry and equation; Dharmendra Tripathi: Review and editing, ensuring clarity. All authors reviewed and approved the final version of the manuscript.

Availability of Data and Materials: Data available within the article. The authors confirm that the data supporting the findings of this study are available within the article.

Ethics Approval: This study does not involve any human participants or animals and therefore did not require ethical approval.

Conflicts of Interest: The authors declare no conflicts of interest.

Nomenclature

Symbol	Description	Unit
a_1, a_2	Amplitudes of the left and right walls	m
c	Propagation velocity	m/s
C	Solute concentration	mol/m^3
d_1, d_2	Dimensional width of the channel	–
D_B	Brownian diffusion	m^2s^{-1}
D_S	Solute diffusivity	m^2s^{-1}

(Continued)

(continued)

Symbol	Description	Unit
D_T	Thermophoretic diffusion	$m^2s^{-1}K^{-1}$
D_{CT} , D_{TC}	Soret and Dufour coefficients	K^{-1} and m^2s^{-1}
Da	Darcy Number	–
F	Mean flow rate	–
Fr	Froude Number	–
g	Gravitational acceleration	m/s^2
G_c	Solutal Grashof Number	–
G_f	Nanoparticle Grashof Number	–
G_r	Grashof Number	–
k	Thermal conductivity	$W/m \cdot K$
k_0	Permeability parameter	H/m
k_r	Rosseland mean absorption coefficient	m^2/mol
l_1, l_2, l_3, l_4	Velocity, temperature, solutal, nanoparticle slip parameters	–
M	Hartmann Number	–
N_b	Brownian motion parameter	–
N_t	Thermophoresis parameter	–
NCT , NTC	Soret and Dufour effects	–
Nu	Nusselt Number	–
p	Dimensionless pressure	–
Pr	Prandtl Number	–
Q	Volumetric flow rate	–
Q_0	Heat source/sink parameter	$m\text{-}^2s^{-3}$
Re	Reynolds Number	–
Rn	Thermal radiation parameter	–
Sc_1	Schmidt number	–
Sc_2	Nanofluid Schmidt number	–
Sh	Sherwood Number	–
t	Time	s
T	Temperature	K
u, v	Velocity components	m/s
We	Weissenberg Number	–
β	Heat source/sink parameter	–
β_T , β_C	Thermal and solutal expansion coefficients	K–1
γ	Nanoparticle concentration	–
λ	Wavelength	m
μ	Dynamic viscosity	$kg/m \cdot s$
μ_0	zero shear rate viscosity	$kg/m \cdot s$
ρ_f , ρ_{f0}	Fluid density and reference density	kg/m^3
ρ_p	Nanoparticle density	kg/m^3
σ	Solutal concentration	–
$\sigma*$	Stefan–Boltzmann constant	W m−2K−

(Continued)

(continued)

Symbol	Description	Unit
θ	Dimensionless temperature	–
Θ	Nanoparticle volume fraction	–
τ_w	Skin friction	–
ψ	Stream function	–
Machine Learning Terms		
ANN	Artificial Neural Network	–
DT	Decision Tree	–
LR	Logistic Regression	–
LRG	Linear Regression	–
ML	Machine Learning	–
NB	Naive Bayes	–
RF	Random Forest	–
SVM	Support Vector Machine	–

References

1. Akram S, Athar M, Saeed K, Umair MY, Muhammad T. Mechanism of double diffusive convection due to magnetized Williamson nanofluid flow in tapered asymmetric channel under the influence of peristaltic propulsion and radiative heat transfer. Int J Num Meth Heat Fluid Flow. 2024;34(2):451–72. doi:10.1108/hff-04-2023-0169.
2. Nadeem S, Akram S. Peristaltic flow of a Williamson fluid in an asymmetric channel. Commun Nonlinear Sci Numer Simul. 2010;15(7):1705–16. doi:10.1016/j.cnsns.2009.07.026.
3. Malik MY, Bilal S, Salahuddin T, Rehman KU. Three-dimensional Williamson fluid flow over a linear stretching surface. Math Sci Lett. 2017;6(1):53–61. doi:10.18576/msl/060109.
4. Farooq N, Hussain A. Peristaltic analysis of Williamson blood flow model with solar biomimetic pump. Int Commun Heat Mass Transf. 2022;138(4):106305. doi:10.1016/j.icheatmasstransfer.2022.106305.
5. Nadeem S, Hussain ST. Flow and heat transfer analysis of Williamson nanofluid. Appl Nanosci. 2014;4(8):1005–12.
6. Akbar NS, Maraj EN, Nadeem S. Investigation of peristaltic flow of Williamson nanofluid in a curved channel with compliant walls. Appl Nanosci. 2014;4(5):511–21. doi:10.1007/s13204-013-0234-9.
7. Krishnamurthy MR, Prasannakumara BC, Gireesha BJ, Gorla RSR. Effect of chemical reaction on MHD boundary layer flow and melting heat transfer of Williamson nanofluid in porous medium. Eng Sci Technol Int J. 2016;19(1):53–61. doi:10.1016/j.jestch.2015.06.010.
8. Eldabe NT, Abo-Seida OM, Abo Seliem AA, Elshekhipy AA, Hegazy N. Magnetohydrodynamic peristaltic flow of Williamson nanofluid with heat and mass transfer through a non-Darcy porous medium. Microsyst Technol. 2018;24(9):3751–76. doi:10.1007/s00542-018-3835-0.
9. Nadeem S, Hussain ST, Lee C. Flow of a Williamson fluid over a stretching sheet. Braz J Chem Eng. 2013;30(3):619–25. doi:10.1590/s0104-66322013000300019.
10. Hashim, Khan M, Hamid A. Convective heat transfer during the flow of Williamson nanofluid with thermal radiation and magnetic effects. Eur Phys J Plus. 2019;134(2):50. doi:10.1140/epjp/i2019-12473-9.
11. Alharbi KAM, Eldin SM, Akgul A. Investigation of Williamson nanofluid in a convectively heated peristaltic channel and magnetic field via method of moments. AIP Adv. 2023;13(6):065313. doi:10.1063/5.0141498.
12. Akram S, Afzal Q. Effects of thermal and concentration convection and induced magnetic field on peristaltic flow of Williamson nanofluid in inclined uniform channel. Eur Phys J Plus. 2020;135(10):857. doi:10.1140/epjp/s13360-020-00869-9.

13. Chakradhar K, Nandagopal K, Prashanthi V, Parandhama A, Somaiah T, Thrinath BVS, et al. MHD effect on peristaltic motion of Williamson fluid via porous channel with suction and injection. Partial Differ Equ Appl Math. 2025;13(2):101103. doi:10.1016/j.padiff.2025.101103.
14. Al-Khafajy DGS. Influence of MHD and wall properties on the peristaltic transport of a williamson fluid with variable viscosity through porous medium. Iraqi J Sci. 2017;58(2C):1076–89. doi:10.24996/ijs.2017.58.2c.11.
15. Riaz A, Alolaiyan H, Razaq A. Convective heat transfer and magnetohydrodynamics across a peristaltic channel coated with nonlinear nanofluid. Coatings. 2019;9(12):816. doi:10.3390/coatings9120816.
16. Makinde OD, Gnaneswara Reddy M, Venugopal Reddy K. Effects of thermal radiation on MHD peristaltic motion of Walters-B fluid with heat source and slip conditions. J Appl Fluid Mech. 2017;10(4):1105–12. doi:10.18869/acadpub.jafm.73.241.27082.
17. Ramesh K, Devakar M. Peristaltic transport of MHD Walters B fluid through porous medium with heat transfer. Iranian J Sci Technol Trans A: Sci. 2017;41(2):489–504. doi:10.1007/s40995-017-0255-4.
18. Reddappa B, Parandhama A, Sreenadh S. Peristaltic transport of conducting Williamson fluid in a porous channel. J Math Comput Sci. 2019;10(2):277–88.
19. Ravikumar S, Makinde OD. Microrotation and shear stress modulation in thermo-solutal convection through micropolar fluid undergoing peristaltic transport with cross-diffusion and thermohydrodynamic effects. Multis Multidiscip Model Exper Des. 2025;8(9):1–22. doi:10.1007/s41939-025-00987-w.
20. Ramesh K, Devakar M. Peristaltic transport of MHD Williamson fluid in an inclined asymmetric channel through porous medium with heat transfer. J Central South Univ. 2015;22(8):3189–201. doi:10.1007/s11771-015-2856-4.
21. Vajravelu K, Sreenadh S, Rajanikanth K, Lee C. Peristaltic transport of a Williamson fluid in asymmetric channels with permeable walls. Nonlin Anal: Real World Appl. 2012;13(6):2804–22. doi:10.1016/j.nonrwa.2012.04.008.
22. Kavitha A, Reddy RH, Sreenadh S, Saravana R. Peristaltic flow of a Williamson fluid in an asymmetric channel through porous medium. Int J Innovat Technol Creat Eng. 2011;1(1):48–53.
23. Aly EH, Ebaid A. Effect of the velocity second slip boundary condition on the peristaltic flow of nanofluids in an asymmetric channel: exact solution. Abst Appl Anal. 2014. doi:10.1155/2014/191876.
24. Hayat T, Bibi S, Rafiq M, Alsaedi A, Abbasi FM. Effect of an inclined magnetic field on peristaltic flow of Williamson fluid in an inclined channel with convective conditions. J Magn Magn Mater. 2016;401:733–45. doi:10.1016/j.jmmm.2015.10.107.
25. Aich W, Javid K, Ghachem K, Ullah I, Iqbal MA, Khan SU, et al. Thermal and physical impact of viscoplastic nanoparticles in a complex divergent channel due to peristalsis phenomenon: heat generation and multiple slip effects. Heliyon. 2023;9(7):e17644. doi:10.1016/j.heliyon.2023.e17644.
26. Akbar NS, Nadeem S, Khan ZH. Thermal and velocity slip effects on the MHD peristaltic flow with carbon nanotubes in an asymmetric channel: application of radiation therapy. Appl Nanosci. 2014;4(7):849–57. doi:10.1007/s13204-013-0265-2.
27. Akbar NS, Hayat T, Nadeem S, Obaidat S. Peristaltic flow of a Williamson fluid in an inclined asymmetric channel with partial slip and heat transfer. Int J Heat Mass Transf. 2012;55(7–8):1855–62. doi:10.1016/j.ijheatmasstransfer.2011.11.038.
28. Alolaiyan H, Riaz A, Razaq A, Saleem N, Zeeshan A, Bhatti MM. Effects of double diffusion convection on third grade nanofluid through a curved compliant peristaltic channel. Coatings. 2020;10(2):154. doi:10.3390/coatings10020154.
29. Tripathi D, Prakash J, Reddy MG, Misra JC. Numerical simulation of double diffusive convection and electroosmosis during peristaltic transport of a micropolar nanofluid on an asymmetric microchannel. J Therm Anal Calorim. 2021;143(3):2499–514. doi:10.1007/s10973-020-10214-y.
30. Sushma S, Samuel N, Neeraja G. Numerical study on double diffusive convective flow of Williamson fluid over a vertical wall. Int J Appl Comput Math. 2021;7(4):148. doi:10.1007/s40819-021-01081-8.
31. Mohamed RA, Abo-Dahab SM, Abd-Alla AM, Soliman MS. Magnetohydrodynamic double-diffusive peristaltic flow of radiating fourth-grade nanofluid through a porous medium with viscous dissipation and heat generation/absorption. Sci Rep. 2023;13(1):13096. doi:10.1038/s41598-023-39756-5.

32. Saeed K, Akram S, Athar M, Razia A, Muhammad T, Alghamdi HA. Mechanism of double-diffusive convection on peristaltic transport of thermally radiative Williamson nanomaterials with slip boundaries and induced magnetic field: a bio-nanoengineering model. Nanomaterials. 2023;13(5):941. doi:10.3390/nano13050941.
33. Bathmanaban P, Siva EP, Santra SS, Askar SS, Foul A, Nandi S. Correction: heat and mass transfer in double-diffusive mixed convection of Casson fluid: biomedical applications. Colloid Polym Sci. 2024;302(11):1855–5.
34. Paandurangan B, Errappa Parthasarathy S, Tripathi D, Bég OA. The impact of double-diffusive convection on electroosmotic peristaltic transport of magnetized Casson nanofluid in a porous asymmetric channel. ZAMM-J Appl Mathem Mech/Zeitschrift Für Angewandte Mathematik Und Mechanik. 2024;104(9):e202300771. doi:10.1002/zamm.202300771.
35. Bilal S, Akram S, Athar M, Saeed K, Razia A, Riaz A. Numerical analysis on theoretical model of magneto-Williamson nanofluid in relation to viscous dissipation, double-diffusion convection, thermal radiation and multiple slip boundaries. Pramana. 2024;98(3):125. doi:10.1007/s12043-024-02798-z.
36. Priyadharshini P, Karpagam V. Machine learning impact of radiative blood flow over a wedge in a time-dependent MHD Williamson fluid. Ann Mathem Comput Sci. 2024;22:12–44. doi:10.56947/amcs.v22.275.
37. Sheth V, Tripathi U, Sharma A. A comparative analysis of machine learning algorithms for classification purpose. Procedia Comput Sci. 2022;215(3):422–31. doi:10.1016/j.procs.2022.12.044.
38. Shafiq A, Çolak AB, Sindhu TN, Al-Mdallal QM, Abdeljawad T. Estimation of unsteady hydromagnetic Williamson fluid flow in a radiative surface through numerical and artificial neural network modeling. Sci Rep. 2021;11(1):14509. doi:10.1038/s41598-021-93790-9.
39. Alzahrani AO, Imran A, Alghamdi AM, Alarood AA, Bahaddad AA, Abdel-Khalek S. Intelligent deep learning analysis of MHD williamson ternary hybrid nanofluid thin film transport with heat and mass transfer under multiple slip effects. Case Stud Therm Eng. 2025;74(2):106810. doi:10.1016/j.csite.2025.106810.
40. Abbasi I, Arshad Z, AlFaify S, Shah Z, Khan WA, Muhammad T. Artificial intelligence analysis of nonlinear radiative and chemically reactive Williamson nanofluid flow with motile microorganisms. J Therm Anal Calorim. 2025;150(25):20653–78. doi:10.1007/s10973-025-14974-3.
41. Abbas Z, Mahmood I, Batool S, Shah SAA, Ragab AE. Evaluation of thermal radiation and flow dynamics mechanisms in the Prandtl ternary nanofluid flow over a Riga plate using artificial neural networks: a modified Buongiorno model approach. Chaos, Solit Fract. 2025;193(2):116083. doi:10.1016/j.chaos.2025.116083.
42. Shah SAA, Alshammari FS, Malik MF, Batool S. Numerical-ANN framework for thermal analysis of MHD water-based prandtl nanofluid flow over a stretching sheet using Bvp4c. Symmetry. 2025;17(8):1347. doi:10.3390/sym17081347.
43. Jangid S, Kolla K. Artificial neural network modeling of natural convection Williamson fluid flow with magnetic and Soret effects in a vertical channel. Eur Phys J Spec Top. 2026;234(23):7421–42. doi:10.1140/epjs/s11734-025-02005-z.
44. Min Z, Shaheen S, Arain MB, Zeeshan A, Hussein HS. AI-based analysis of heat transfer in Williamson nanofluids over a vertically stretching sheet. Int J Hydrogen Energy. 2026;208(1):153383. doi:10.1016/j.ijhydene.2026.153383.
45. Vinutha K, Varun Kumar RS, Raghavendra Rao PS, Kulshreshta A, Chohan JS, Abdulrahman A. Nonsimilar solutions for williamson nanofluid flow influenced by chemical reactions due to generated and absorbed heat by finite element method. Nano. 2026;21(1):2550041. doi:10.1142/s1793292025500419.
46. Hanumantha H, Keriyappa S, Mulimani M, Chamkha AJ, Srinivasa K, Kolasani S, et al. Thermal and flow characteristics of MHD Williamson hybrid nanofluid under activation energy in a porous asymmetrical peristaltic channel. Trans Comput Model Intell Syst. 2026;3:10059. doi:10.65112/tcmis.10059.
47. Ashique A, Shah NA, Afzal U, Alawaideh Y, Abdal S, Chung JD. Artificial neural network-based flow and heat transfer analysis of williamson nanofluid over a moving wedge: effects of thermal radiation, viscous dissipation, and homogeneous-heterogeneous. Comput Model Eng Sci. 2026;146(2):22. doi:10.32604/cmes.2025.073292.